This is a preprint, the final version is subject to change, of the American Mineralogist (MSA)
Cite as Authors (Year) Title. American Mineralogist, in press.
DOI: https://doi.org/10.2138/am-2020-7007

7007R: Correction date 12/16/2019

Texture constraints on crystal size distribution methodology: An application to the Laki fissure eruption

Kim A. Cone,[1*] Richard F. Wendlandt[1], Katharina Pfaff[1], Omero F. Orlandini[2]

[1]Department of Geology and Geological Engineering, Colorado School of Mines, 1516 Illinois Street, Golden, Colorado, 80401, U.S.A.

[2]Geological Sciences, University of Colorado Boulder, UCB 399, Boulder, Colorado, 80309, U.S.A.

*Corresponding author: Department of Geology and Geological Engineering, Colorado School of Mines, Golden, Colorado, 80401, U.S.A.

Email: kimacone@gmail.com

Number of words (abstract): 322

Number of words (post-abstract and pre-reference sections): 8374

Kim A. Cone kcone@mines.edu

Richard F. Wendlandt rwendlan@mines.edu

Katharina Pfaff kpfaff@mines.edu

Omero F. Orlandini omero.orlandini@colorado.edu

ABSTRACT

Modelling crystal size distributions often requires the extraction of 2D discrete crystal lengths in order to calculate 3D volumetric equivalences. These apparent lengths are obtained from digital images that exploit different physical and chemical characteristics of samples, and the choice of image type can affect the interpretation of crystal length measurements, thus affecting crystal size distribution modelling. To examine method- and texture-based effects on extracting crystal size distributions, we obtained plagioclase length measurements from two basaltic lava samples with different phenocryst volumes and contiguity styles, from the well-documented Laki fissure eruptions of 1783-1784. Using approaches that consider inherent texture-based limitations of 2D image types, we employed manual tracing and imaging software to extract plagioclase crystal lengths from three types of images: 1) photomicrographs from polarized-light microscopy, 2) backscatter electron images from scanning electron microscopy, and 3) energy-dispersive X-ray maps from automated mineralogy. Our results demonstrate that 1) phenocrysts ($L \geq 150$ μm) and groundmass plagioclase ($L < 150$ μm) in our basalt samples appear with multiple aspect ratios, while the latter also display greater nucleation densities as crystal size population are continuously refined over increasingly smaller crystal lengths; 2) complex crystal clusters must be manually dissected into their discrete crystal components to produce meaningful crystal size distributions; 3) localized electron backscatter diffraction analysis reveals mild preferred orientation in complex clusters and groundmass, the latter confirmed by variations in crystal size distributions between orthogonal backscatter electron images; and 4) method-induced variations in both aspect ratio and crystal length determination can produce a wide range of kinetic interpretations that pose challenges for cross-research comparisons. For phenocrysts, compensating for clustering and fracturing through manual tracing remains the most effective method, while groundmass populations can be addressed with high-resolution (micron-scale) automated scanning electron microscopy for deciphering late-stage eruptive behavior. A texture-focused protocol should be established, as any kinetic information derived from crystal size distribution analyses across multiple studies employing multiple approaches cannot otherwise be directly compared.

Keywords: plagioclase, crystal size distributions, aspect ratio, basalt, textural analysis, crystallization kinetics, automated mineralogy, EBSD, Laki

INTRODUCTION

Textural analysis of volcanic rock provides insight into crystallization dynamics and associated magmatic environments. Petrologic studies that focus on geochemistry and phase equilibria as the primary means to explore geologic questions can utilize texture to constrain crystallization histories and the extent to which crystallization reflects dynamic processes such as fractionation or magma mixing. A common textural investigative tool is the use of crystal size distributions (CSDs) that focus on the most conspicuous aspect of texture – the distribution of crystal sizes (Cashman and Marsh, 1988; Marsh, 1988, 1998; Higgins, 2000, 2006).

Crystal size distributions for a purely open, steady-state igneous system display a linear relationship between the natural logarithm of crystal population density and the corresponding crystal size, L (Marsh, 1988). Natural lava samples variably mimic this relationship through seriate textures where crystals nucleate and grow through size populations. This is mathematically and graphically represented by the following power law equation:

$$n(L) = n^0 e^{-(L/G\tau)} \qquad (1)$$

where $n(L)$ is the population density for crystals of size L (the 3D length, usually converted from 2D thin section measurements), G is the average crystal growth rate (assumed constant and derived from experimental values (Kirkpatrick, 1977; Cashman and Marsh, 1988; Cashman, 1993)), τ is the residence time, and n^0 is the nucleation density. Other characteristics may be determined from the equation: characteristic length (i.e. average size, C) can be calculated as $G\tau$, an associated regression slope as $-1/C$, and nucleation rate (J) is equivalent to n^0G. Semilogarithmic plotting of population density on the y-axis against corresponding size on the x-axis produces a negatively sloped linear expression. For the population density, the crystal count in each bin from the x-axis is divided by the analyzed area of the thin section on a vesicle-free basis. That value is further divided by the bin width. The result is a population density unit of mm^{-4}. Deviations from this ideal, negative linear slope indicate disruptions to a kinetically-driven system defined by constant nucleation and crystal growth, suggesting one or more crystal populations with different nucleation and growth histories. Geologic context would then dictate probable causes for these deviations.

Various aspects of CSD analysis have been examined over the last 30 years since the seminal works of Marsh (1988) and Cashman and Marsh (1988) on the Makaopuhi lava lake, having adapted the idea of crystal population balance from chemical engineering (Randolph and Larson, 1971) to igneous systems. Recent topics include confocal microscopy and microlite measurement in thin section (Castro et al., 2003), stereological corrections concerning cut section effects and intersection probability effects (Higgins, 2000, 2006; Mock and Jerram, 2005; Morgan and Jerram, 2006), decompression-induced twinning in plagioclase microlites as revealed by electron backscatter diffraction (EBSD) analysis (Brugger and Hammer, 2015), and most recently the use of automated mineralogy in obtaining CSDs from plagioclase populations in a large volume lava eruption (Neave et al., 2017). There is no established protocol for obtaining crystal size distributions for igneous rock, although certain approaches are shared across studies. Ideally, solid and intact whole-crystals would be removed from a sample and individual crystal volumes determined directly in order to establish a proper CSD (Higgins, 2006). This approach is impractical for most igneous studies and so petrographic thin sections or grayscale backscatter electron (BSE) images often serve as a starting point for extraction of 2D crystal sizes that are then converted to 3D volumetric equivalents. These conversions involve stereological approaches that are also not consistently applied across studies.

The purpose of this work is to explore CSDs using multiple types of imaging techniques for two texturally different basaltic lavas from the historic Laki fissure eruptions. We utilize both manual tracing and four types of digital images in conjunction with imaging software to examine plagioclase crystal length and width measurements, some of which are used to construct CSDs that reflect the separation of discrete crystals from glomerocrysts. In related published works, phenocrysts that exist as members of either monomineralic or polymineralic clusters have been treated for the purpose of manual tracing as single entities (i.e. the entire cluster is traced as a single crystal), which they are clearly not (Cashman and Marsh, 1988; Neave et al., 2013).

Textural considerations for CSD analysis

Determining CSDs requires multiple considerations: 1) crystal measurement methods, 2) cut-section effects, 3) intersection-probability effects, 4) crystal aspect ratios, 5) sufficient sample counts, 6) crystal contiguity, 7) crystal fracturing, 8) crystallographic preferred orientation (CPO), and 9) growth rates (Higgins, 2006). Crystal measurements involve variations of longest-length lines or bounding boxes, and length-extraction methods should be based on crystal shapes (Higgins, 2006). Cut-section effects (greatest-length measurements rarely reflect the actual maximum size of a crystal) and intersection-probability effects (smaller crystals are less likely to be intersected than larger ones) are mathematically treated by programs such as CSDCorrections (Higgins, 2000, 2006). Crystal aspect ratios become increasingly important in CSDs the more crystal shapes deviate from a perfect sphere, and CSDSlice is frequently employed to determine a statistical best-fit aspect ratio for a group of crystal measurements based on 10,000 random cuts through > 700 crystal shapes (Morgan and Jerram, 2006). Aspect ratios are a strong function of crystallization time and cooling rate, as demonstrated by Holness (2014) for plagioclase in both basaltic doleritic and extrusive textures, and reflect differential growth rates on plagioclase crystal faces. Sufficient crystal counts are also required for proper aspect ratios, and at least 75 crystal sections are required in order to determine a robust best-fit aspect ratio for tabular crystals and at least 250 crystal sections for acicular ones (Morgan and Jerram, 2006). Crystal contiguity (i.e. touching crystals) and crystal fracturing impose opposite effects on crystal counts; the former introduces inflated counts of larger crystals while the latter creates an inflated number of smaller crystals. Both aspects can be addressed to some extent by ImageJ imaging software (Schneider et al., 2012), but due to variability in fracture widths a single filling-in protocol does not adequately address all fracture gap-widths, although manual tracing of a single bounding outline around multiply-fractured crystals adequately addresses this issue. Crystallographic preferred orientation is often visually estimated and treated as random for the purpose of a study in absence of obvious foliation. Orientation effects are one of the least investigated aspects of CSD analysis as they are potentially one of the most difficult and expensive to quantify; properly deciphering the extent of CPO involves electron backscatter diffraction (EBSD) analysis with carefully polished samples using colloidal silica and can be impractical depending on scan-time versus scan-resolution costs. Crystal growth rates pose another challenge to untangling CSDs, as changing degrees of undercooling can force varying growths rates that are then crystallographically controlled (Holness, 2014 and references therein). Plagioclase growth rates have been estimated for low degrees of undercooling as well as for decompression-induced conditions (Hammer et al., 1999; Orlando et al., 2008; Shea and Hammer, 2013), but choosing a single growth rate for a system a priori is not a straightforward process, as multiple growth rates may have been in effect.

Image considerations for CSD analysis

The most frequently used types of images for crystal measurements are thin section photomicrographs and BSE images. The latter are generated from scanning electron microscopy (SEM) and reflect increasing material atomic weight through increasing grayscale image brightness. SEM-EDS (energy-dispersive X-ray spectroscopy) imaging is less frequently used and relies on characteristic X-rays produced within an interaction volume of a sample to produce a false-color elemental distribution map.

Thin section photomicrographs are the least expensive but potentially the most time-consuming starting image. Manual tracing requirements vary depending on image resolution and the crystal size populations being considered. The digitized tracings or markings are converted to length measurements using software such as ImageJ. The advantage to using thin section images is that manual markings permit user control over crystal fracturing, contiguity issues can be simultaneously addressed by the user manually, and the separation of glomerocrysts into discrete crystals. A potential disadvantage is tied to resolution, where fine-grained groundmass-sized crystals (particularly anhedral ones) may not be readily discernible in lower-resolution images. As with all images, resolution dictates the smallest crystal size populations capable of being analyzed.

BSE and EDS images may also be processed through ImageJ to obtain crystal length measurements without the addition of manual tracing or markings. Since BSE images are grayscale, color threshold adjustments may be required to prevent grayscale overlap between the mineral of interest and another with similar atomic weight. Unlike thin section images where plagioclase twinning patterns in a cluster help discern discrete crystals for tracing, grayscale BSE images frequently produce a single grayscale entity where crystal borders are not readily apparent, particularly in the absence of zoning. Detecting crystal borders within clusters is also problematic with EDS imaging if plagioclase composition is identical among contiguous crystals. As crystal clusters are common in volcanic textures, a greater frequency of clusters will artificially increase larger crystal size counts. Another less frequently used method, electron backscatter diffraction, can detect discrete crystals by proximal offsets in crystal orientation but can also produce an overinflated number of crystals within a crystal cluster if twinning is not properly accounted for.

Plagioclase in CSD analysis

Plagioclase is a ubiquitous mineral phase in mafic lavas and serves as a sensitive fingerprint of changes in melt conditions and in physical processes (e.g. magma mixing and crystal settling). Because plagioclase often nucleates and grows over wide and fluctuating temperature and pressure regimes during the eruptive process, polydisperse populations (multiple true sizes) and multiple aspect ratios are common in volcanic products (Guilbaud et al., 2007; Neave et al., 2013) and can reflect different cooling rates (Brugger and Hammer, 2010 and references therein; Holness, 2014). Fast-cooling upon eruption often produces anhedral plagioclase microlites (Brugger and Hammer, 2015) with swallowtail morphology and twinning styles that may point to conditions of crystallization and growth histories (Xu et al., 2016). Multiple plagioclase habits in a single sample are often treated with stereological corrections in order to produce meaningful CSDs, as true crystal lengths that represent actual 3D crystal volumes are not directly represented in 2D thin sections (Morgan and Jerram, 2006).

EBSD and automated mineralogy

Large-scale, high-resolution SEM-based EDS images can be efficiently acquired from automated systems (i.e. automated mineralogy). The user defines the area on a polished sample to be scanned at a chosen resolution. The final pixel-based, large-scale image comprises multiple scanned fields that are automatically stitched together. Each pixel represents elemental information that can be used to produce associated mineral images (Gottlieb, 2000). The mineral images are then employed as crystal images from which lengths can be extracted. The user must first establish a reliable protocol for defining the mineral (either a stoichiometric formula or one based on an actual geochemical analysis) and once completed, the protocol can be reused for the same phase from multiple samples (the protocol for defining plagioclase for our samples is explained the methods section). The early use of automated SEM-based approaches focused on mineral processing and ore identification in an attempt to optimize ore release from natural samples (Sutherland, 2007; Gu, 2003). Today, these approaches have become increasingly routine in mineralogical and petrological analyses (Hrstka et al., 2018). In this research, the TIMA (Tescan Integrated Mineral Analyser) automated mineralogy system is employed to produce images from which plagioclase crystal lengths are obtained. Automated mineralogy produces plagioclase images based on elemental composition whereas EBSD produces information based on crystallographic orientation.

THE LAKI FISSURE ERUPTIONS OF 1783-1784

The eight-month long tholeiitic fissure eruptions in the Eastern Volcanic Zone of Iceland lasted from June 8, 1783 to February 7, 1784 and produced ~15.1 km^3 of lava, covering 565 km^2 (Thordarson and Self, 1993). Ten separate eruptions coincided with the opening of one of ten partially-overlapping, en-echelon fissures, produced as a result of spreading between the North American and European plates (Thordarson and Self, 1993; Fig. 1). Earthquake swarms began in May of 1783 as the fissure system propagated northeast toward Grímsvötn, followed by the first eruptive episode in June. The ten discrete eruptive episodes were recorded based on preserved tephra deposits, stratigraphy, and historical accounts, with each episode experiencing an initial stage of phreatomagmatic explosivity caused by the high position of the water table. Eruptive styles changed to sub-Plinian and then to Hawaiian activity as the water table lowered (Thordarson and Self, 1993). The first five episodes (and hence the first five fissures) occurred on the southwest side of Laki mountain and produced magma that discharged toward the south within the Skaftá river gorge. The last five episodes occurred on the northeast side of Laki mountain and were channeled southward within the Hverfisfljót river gorge. A detailed description of the Laki eruption characteristics is provided by Thordarson and Self (1993).

The geochemical characteristics are well-constrained across multiple studies for the Laki region (Bindeman et al., 2006; Guildbaud et al., 2007; Passmore et al., 2012; Neave et al., 2013; Neave et al., 2017). Passmore et al. (2012) concluded that crystal mush entrainment was greater on average at later stages of the eruption, coinciding with the presence of anorthitic plagioclase (Passmore et al., 2012; Neave et al., 2013). Neave et al. (2013) found evidence of concurrent mixing and crystallization of different sources.

SAMPLE CHARACTERISTICS

Two samples (L-4B and L-E) were collected along roadways F206 and Route 1 (Fig. 1), representing micro-porphyritic basalt from both the first and second halves of the eight-month long Laki eruption. L-4B is groundmass-dominant and proximal to its originating fissure, produced during the first half (i.e. the first five eruptions). L-E is seriate and a distal-to-fissure sample, produced during the second half. Both samples are dominated by plagioclase, clinopyroxene, olivine and dendritic opaques. Dendritic titanomagnetite only occurs in the groundmass while plagioclase, clinopyroxene and olivine occur as both phenocryst and groundmass. Sample L-4B is volumetrically dominated by the finest groundmass and provides the starkest contrast between phenocryst and groundmass crystal population sizes, appearing strongly bimodal (Fig. 2). L-E contains the largest phenocrysts and the coarsest groundmass, with a sub-seriate crystal population (Fig. 3). Because a central focus of this paper concerns how groundmass-dominated and phenocryst-dominated textures shape CSD curves, L-4B and L-E are highly suitable as they represent two end-members of volcanic texture. Based on initial optical microscopy observations, L-4B contains discrete plagioclase phenocrysts up to ~0.70 mm, close to that of L-E's maximum crystal length of ~ 0.80 mm. In both samples, the dominant shape of discrete plagioclase phenocrysts is subhedral to euhedral. Plagioclase-only whole-clusters attain maximum lengths of up to ~3.5 mm in L-E and ~2.0 mm in L-4B. For clusters with plagioclase and clinopyroxene (with or without olivine), whole-cluster lengths were slightly smaller in L-4B. Tables 1 and 2 summarize the major phenocryst occurrences for both samples.

MATERIALS AND THIN SECTION PREPARATION

Two orthogonally-oriented thin sections were prepared from each of the two lava samples. Group-A thin sections (L-4B and L-E) consisted of the original cut surface from their respective hand sample while Group-B thin sections (V4 and V1) consisted of lengthwise orthogonal cuts produced from the remaining billets of group A (Supplemental Fig. 1). If a foliated fabric exists, then orthogonal cuts can assist in the detection of crystal preferred orientation when statistically significant similarities (or differences) in CSDs are present (see "BSE imaging to detect preferred orientation" in the methods section). Proximal orthogonal cuts (cuts obtained from immediately adjacent portions of a sample) can also assist in detecting localized fabric variations when analysis is performed along the same regions between the original and orthogonally prepared thin section. L-E and L-4B were prepared by Wagner Petrographic, Utah and polished to 0.25 μm. L-E also incurred a final polish with 0.05 μm colloidal silica for ~20 hours on a Buehler Vibromet 2 vibratory polisher at 70% amplitude at the University of Wyoming's Material Characterization Laboratory. Thin sections V1 and V4 were prepared by the Colorado

School of Mines' Thin Section Laboratory and polished with 0.05 μm alumina. All thin sections were carbon coated using a Cressington 208 carbon coater to prevent charging during scans.

METHODS

Overview for determining crystal size distributions

Crystal size distribution measurements began with the acquisition of plagioclase crystal length measurements from three general types of digital images: 1) photomicrographs, 2) BSE images, and 3) two types of automated mineralogy images. Adobe Photoshop CC was used for manual tracing where noted. All three image types were then imported into ImageJ open source software and converted to 8-bit and grayscale thresholded for crystal length measurements. ImageJ measurements were recorded in a spreadsheet and imported into CSDSlice (where indicated), a program that determines statistical best-fit aspect ratios for a group of length measurements (Morgan and Jerram, 2006). The five most statistically significant aspect ratios (the five greatest R^2 values) are returned in the form x: y: z, representing the short (S), intermediate (I), and long (L) axes ratios. At least 75 crystal sections are required in order to determine a robust best-fit aspect ratio for tabular crystals and at least 250 crystal sections for acicular ones (Morgan and Jerram, 2006). CSDSlice determines aspect ratio from best-fit ellipse measurements and has been previously used for plagioclase (Brugger and Hammer, 2010; Neave et al. 2013; 2017). Because plagioclase can acquire multiple shapes reflecting unique undercoolings, larger-crystal populations were stereologically addressed separately from smaller-crystal populations (Morgan and Jerram, 2006). Crystals were analyzed as at least two distinct populations in CSDSlice, separated by a size threshold of 150 μm as determined by previous research of Laki lavas (Passmore et al., 2012; Neave et al, 2013).

There are multiple approaches for obtaining initial apparent length measurements from a 2D cut section with the final goal that the measurements serve as the best proxy for actual 3D crystal volumes. Most methods of defining linear 2D measurements produce similar values for equant shapes but values begin to diverge with decreased symmetry (Higgins, 2006). The long axis of a best-fit ellipse serves as a strong proxy for actual size, *L*, (Higgins, 2006) assuming a random fabric and non-spherical shapes. Plagioclase length measurements from ImageJ were recorded in an Excel spreadsheet along with aspect ratios from CSDSlice. Both sets of data were input into CSDCorrections (Higgins, 2000, 2006). CSDs are partly determined based on bin widths that can be adjusted from two to ten bins per decade (i.e. per log unit, or factor of 10) in CSDCorrections. Here, we use a minimum of five bins per decade (unless stated otherwise) to reduce uncertainty attributed to either using an increased number of smaller bins or to having an insufficient sample population.

Using orthogonal BSE images to detect preferred orientation

For thin sections L-4B and its orthogonal equivalent V4, both groundmass-dominated, a total of three proximal BSE-image pairs (Supplemental Figs. 2, 3, and 4) were acquired at the Colorado School of Mines using a TESCAN MIRA3 LMH Schottky field emission-scanning electron microscope (FE-SEM) equipped with a single-crystal YAG BSE detector and a Bruker XFlash 6/30 silicon drift detector. Scan conditions included an accelerating voltage of 15 kv, a beam intensity of 11, and a working distance of 10 mm. The BSE images were ~300 μm x 250 μm and only plagioclase crystal lengths ≤ 150 μm and ≥ 1 μm were considered for CSD plots. The BSE images were used to perform a relative-fabric analysis. This fabric test consisted of comparing

CSDs between three BSE images from L-4B and three similarly located BSE images from V4 (Supplemental Fig. 2). Orthogonal cut sections are frequently used as a fabric test (Meurer and Boudreau, 1998; Launeau et al. 2005); therefore, if the general fabric is similar across L-4B, cut sections through crystals from the two orthogonal sets, regardless of crystal contiguity, should theoretically produce similar CSDs.

Vesicle borders were avoided to minimize crystal preferred orientation observed on some vesicle walls. This groundmass fabric test involved several assumptions regarding eruptive processes on the scale of grayscale BSE images: late-stage groundmass crystallization occurred as a single pulse; images reflect crystals of similar aspect ratios and corresponding size populations; and crystal contiguity patterns are similar across images if fabric is truly random. To maintain consistency between image-derived length measurements in ImageJ, thresholding reflected a compromise where maximum values preserved plagioclase boundaries (excessive threshold values created artificially large plagioclase particles), but reduced fractures and speckling caused by similar grayscaling of clinopyroxene cores. The maximum upper threshold value was determined visually from ImageJ threshold peaks, at the point where the right tail (upper portion of the threshold curve) for the plagioclase peak displays the largest change in slope. Only particles with major axes $\leq$ 150 μm but $\geq$ 1 μm were considered. Results for both edge-particle exclusion and inclusion were examined. The plagioclase groundmass aspect ratio was set to 1:4:8 (prismatic) and 1:8:8 (tabular) in CSDCorrections, consistent with the minimum length-to-width ratio of >4 reported by Neave et al. (2017). BSE images show that discrete groundmass plagioclase crystals are often contiguous, producing a singly complex, large connected particle that is not acknowledged by ImageJ.

Electron backscatter diffraction (EBSD) imaging

Orientation analysis for a single glomerocryst and surrounding groundmass in sample L-E was completed on a FEI QUANTA FEG 450 field emission scanning electron microscope equipped with an Oxford Instruments X-Max 80 mm^2 EBSD detector and a Centaurus BSE detector at the University of Wyoming's Material Characterization Laboratory. The following scan conditions were used: a sample tilt angle of 70 degrees, an accelerating voltage of 20 kV, a spot size of 5 µm, a step size of 2.5 µm and a working distance of 30 mm. Oxford Instruments HKL Channel 5 software was used for both acquisition and noise reduction. Initial indexing occurred at a Hough transform resolution of 60 with subsequent re-indexings of 70 and 55. Noise reduction was performed after the three re-indexings, following Prior et al. (1999). A mean angular deviation (MAD) of ≥1° was used to define grain boundaries. A freely available MATLAB toolbox called MTEX (version 4.5.1; Mainprice et al., 2015) was used to process the final stitched-and-re-indexed file. The toolbox provides a quantitative fabric descriptor called an M-index, thoroughly discussed in Skemer et al. (2005). An M-index is based on the distribution of misorientation angles and requires ~150 orientation measurements to produce a meaningful result, on a scale of 0 to 1, where 0 indicates no preferred orientation and 1 indicates a strong preferred orientation. MTEX was used to produce orientation data and discrete-crystal boundary maps from Channel 5 files, accounting for the 12 plagioclase twin laws as described by Xu et al. (2016).

Automated mineralogy

Automated mineralogy analysis was performed at the Colorado School of Mines Mineral and Materials Characterization Facility using a TESCAN-VEGA 3 Model LMU VP-SEM with four

PulseTor 30 mm^2 EDS detectors, a YAG scintillator BSE detector, and TIMA software version 1.5.26. Analysis was initiated using the control program TIMA3. Scan conditions included an accelerating voltage of 25 keV and a beam intensity of 14. TIMA phase maps of plagioclase were initially grouped by anorthite content: An_0 – $An_{50,}$ An_{50} – $An_{64,}$ An_{64} – $An_{89,}$ and An_{89} – An_{100}, following the Passmore et al. (2012) definition of a plagioclase groundmass minimum of An_{51} and a maximum of An_{64} and plagioclase phenocryst cores up to An_{89}. Our anorthite contents agree with the above reported values as well as with those reported in Guilbaud et al. (2007), with primitive plagioclase cores >An_{70} and groundmass similar to phenocryst rims of An_{49-70} (lava, not tephra). Neave et al. (2017) also utilize An_{64} as a separator to distinguish between groundmass and phenocryst of Laki basalts. All our samples show less than 40% vesicles (L-4B ~24% and L-E ~16%), as determined by ImageJ thresholding.

Plagioclase was specifically defined for the Laki samples for automated mineralogy analysis by first establishing BSE brightness values from point analysis of plagioclase in the thin sections. Brightness values were determined to range between 19.8 to 22.5% using the TIMA software. Using Bright Phase Search mode, only particles and grains within the above mentioned brightness range were analyzed and an EDS spectrum for each pixel was acquired (1000 X-ray counts per point analysis at a spatial resolution of 2 μm). The EDS spectra are compared against a lookup table allowing a plagioclase composition assignment to be made at each acquisition point. Results are output by the TIMA software as a spreadsheet giving the area percent of each composition in the look-up table as a compositional map. Definitions were created for the degree of anorthite content shown in the groups listed above so that spectra produced images reflecting the grouped anorthite values. Spectra acquisition occurs over multiple smaller fields and TIMA software automatically stitches the fields together to produce the final larger image. The result is a digital image of plagioclase crystals superimposed onto a corresponding BSE image. The false-color image is referred to here as a panoramic, or a panoramic image. Scan times were ~6 hours for L-4B and ~17 hours for L-E.

Two types of automated mineralogy plagioclase images were used to obtain crystal length measurements: 1) “panoramic” false-color images (Supplemental Figs. 6 and 7) and 2) “isolated-particle” images where plagioclase phenocrysts and crystal clusters are automatically digitally isolated from the original false-color image (i.e. from panoramic images). In the case of isolated-particles images, each coherent particle can be further reduced in size by digital clipping, or segmenting (Supplemental Fig. 5). For both types of images, phenocrysts that border image edges appear linearly truncated and were manually deleted. Particles that suggested fracturing and possible loss of area were included in size counts only when at least ~80% of the perceived original size was present. Particles were first ranked by size using TIMA software. Because TIMA calculates size using the diameter of an equal area circle, phenocrysts suitable for length measurements from both TIMA panoramas and isolated-particle images were determined by visual inspection such that the particle rendered an equivalent ~150 μm maximum length (the greatest distance between the two farthest points on a particle outline). The diameters of equal-area circles were ~80 μm for L-4B and ~90 μm for L-E. Long axes of best-fit ellipses were then calculated by ImageJ. Phenocrysts in cross-polarized light (XPL) photomicrograph equivalents of TIMA panoramas were traced, and the long axes of best-fit ellipses were determined with ImageJ.

RESULTS

Orthogonal cuts and BSE fabric assessment

Figures 4 through 6 summarize our findings. L-4B sampled areas show strong similarities in CSD curvature at *L* values < ~25 μm and < ~15 μm for both E (edge-bordering) and NE (non edge-bordering) types of analyses at aspect ratios of 1:4:8 and 1:8:8, respectively (Fig. 4), suggesting that crystal size distributions are similar among the three spatially separated regions within sample L-4B. Edge-bordering analyses produce larger *L* values likely due to the effects of increased contiguity (and not smaller *L* values due to crystal truncation). Divergence of CSDs occur toward the larger *L* values as smaller particles are likely contributing to the contiguity affect and are therefore not counted in smaller-*L* bins. Sampled regions within V4 display similar CSDs but divergence occurs much earlier at ~*L*=10 μm for 1:4:8 and ~*L*=5 μm for 1:8:8.

The BSE image for spot V4_1 (Supplemental Fig. 4) initially suggests a coarser population but the average size, *C*, is 3.37 μm. *C* values for spot V4_2 and spot V4_3 are 3.43 and 3.36 μm, respectively, indicating ~2% maximum difference. Despite the potential contiguity artifacts of thresholding BSE images in ImageJ, CSD curves are remarkably similar in shape for a given aspect ratio, suggesting not only consistency in fabric between L-4B and orthogonal V4, but since the two sections are orthogonal, minimal preferred fabric. The inclusion of edge-particles should theoretically create smaller truncated particles that increase population counts for the smaller *L*-bins into which those truncated particles fall. However, this behavior is not observed consistently, particularly in Figure 4 where E-curves lie both above and below NE-curves and may be an effect of a large crystal sample size. Although growth rate and residence time were not of concern for this analysis, the effects of particle-shape choice on kinetic information is apparent. Figures 5 and 6 show the results of E and NE-style analyses. Figure 5 suggests that variations in CSD curves are more sensitive to the value of aspect ratio (red lines) than to edge effects (black lines), and that nucleation densities approach similar values for a single aspect ratio. Figure 6 shows that combining the six sampled groundmass regions from L-4B and V4 produces a single CSD curve that suggests a common pattern of an increasingly fast-cooling lava where groundmass nucleation rates increase over time, also reflected in the acicularity of groundmass crystals (Shea and Hammer, 2013).

CSDs derived from automated mineralogy (TIMA) and manually traced images: Phenocrysts (*L* ≥ 150 μm)

Scans of plagioclase from L-4B (7% plagioclase phenocrysts) and L-E (10% plagioclase phenocrysts) were initially acquired over 133.406 and 170.208 mm^2 (Table 3) and subsequently cropped for ImageJ analysis, resulting in 92.57 mm^2 (L-4B, 8901 x 2600 pixels) and 163.94 mm^2 (L-E, 3600 x 11387 pixels). Full thin section scans were not performed as acquisition times for L-4B and L-E were already 6+ hours and 17+ hours at a spatial resolution of 2 μm, respectively. Zero-plagioclase pixels occurred in some of the largest phenocrysts and rarely in groundmass crystals. L-4B displayed three major occurrences of regions of non-plagioclase pixels, and this issue was addressed before image processing with ImageJ by manually assigning the missing pixels the same greyscale color as the plagioclase present (Supplemental Fig. 6). L-E was highly porphyritic and contained up to 50 variably affected phenocrysts that were addressed in a similar manner to L-4B (Supplemental Fig. 7).

CSDSlice determined best-fit aspect ratios of 1.0: 3.0: 6.0 (R^2 = 0.6353) and 1.0: 2.5: 5.5 (R^2 = 0.8486) for L-4B phenocrysts using isolated-particle and panoramic images, respectively. The isolated-particle image provided 67 phenocrysts (fewer than the 75 required for robust aspect ratios) while the panorama image provided 422 phenocryst length measurements. Further removal of smaller-size populations of phenocrysts in an attempt to improve the correlation strength of an aspect ratio had the reverse effect, as R^2 values were reduced.

L-E aspect ratios for isolated-particle and panorama images were 1.0: 2.1: 5.5 (R^2 = 0.8153) and 1.0: 2.5: 5.0 (R^2 = 0.8156), respectively. Because L-E is texturally seriate, the populations for both isolated-particle (732 phenocrysts) and panorama (3211 phenocrysts) images were examined for the largest 50% and 25% size subpopulations to determine if there was an improvement in a best-fit shape. R^2 values increased slightly to 0.8206 and 0.8203 for the largest 50% and 25% size sub-populations for the panorama and decreased slightly for isolated-particle images, to 0.8153 and 0.8110 for the same percentiles. All adjustments to phenocryst populations as described above resulted in negligible changes to aspect ratios.

Photomicrograph phenocryst tracings for L-4B and L-E were performed over similar areas compared to automated mineralogy scans (minimum TIMA plagioclase measurements based on a diameter of an equal-area circle were ~45 μm for L-E and ~70 μm for L-4B). Tracings were processed with ImageJ and converted to dimensions of best-fit ellipses. For texturally bimodal L-4B, 291 distinct phenocrysts were traced, and where glomerocrysts existed, individual plagioclase crystals were traced to prevent artifact coarse-size skewing. CSDSlice determined a best-fit aspect ratio of 1.0: 3.6: 7.0 for L-4B with R^2 = 0.8897. For L-E and its strongly seriate

DOI: https://doi.org/10.2138/am-2020-7007

texture, multiple aspect ratios were determined for phenocryst sub-populations. All tracings resulting in long-axes measurements of $L \geq \sim 100$ µm were first analyzed as a single group (1491 crystals), resulting in a best-fit aspect ratio of 1.0: 3.3: 8.0 with $R^2 = 0.8092$. The largest 75% and 50% long-axes sub-populations produced aspect ratios of 1.0: 3.6: 7.0 ($R^2 = 0.8360$) and 1.0: 5.0: 9.0 ($R^2 = 0.8552$), respectively.

Figure 7 summarizes crystal size distributions comparing isolated-particle, panorama, and XPL tracings; resulting kinetic characteristics appear in Table 4. Three aspect ratios were used as determined by each method. Another set of CSDs were produced using crystal lengths from each of the three methods but with the aspect ratio determined from XPL tracing only ("new aspect ratio" in Figs. 7A and 7B).

Discontinuities in CSD curves occurred at the largest L-bins due to an insufficient sample size within those bins. For L-4B (Fig. 7) photomicrograph tracings provided the most consistent and continuous data for all size populations ≥ 150 µm. Isolated-particle images did not provide adequate data points at the coarsest sizes, presumably due to fractured phenocrysts that TIMA post-processing interpreted as multiple smaller particles. Panorama images provided similar small-L bin behavior but, like isolated-particle images, caused CSD discontinuities at the coarsest bins due to phenocryst fracturing. However, the downturn at the finest fractions is preserved by all methods, and so downturns suggest that more sampling is needed below the 150 µm threshold. The use of the photomicrograph-derived aspect ratio with isolated-particle and panorama crystal lengths caused a slight shift of the CSDs to lower L-values. Depending on which portion of the curve a regression line is back-extrapolated from to estimate a nucleation population density, this curve shift may have the effect of slightly reducing the nucleation density but by less than an order-of-magnitude.

L-E CSD curve continuity was maintained due to the large number of measurements. The downturn over small L-values for CSDs from isolated-particle images was likely an artifact of equating the TIMA-defined size of ~80 µm to a 150 µm longest-length measurement. Panorama images provided a similar shape profile to that created from XPL tracing, but the largest particle measurements reflect inflated values due to particle contiguity within plagioclase-dominant glomerocrysts. The panorama-derived curve is smooth compared to the XPL-derived curve and suggests that the former method may have produced an artificially greater number of larger particles, thereby detecting more particles than manual tracing provided, although to what extent artifact crystal counts were produced is uncertain. As with L-4B, minor horizontal shifts in CSDs occurred when the XPL-derived aspect ratio was used.

CSDs derived from automated mineralogy (TIMA) images: Groundmass (L < 150 µm)

Length measurements from manual phenocryst tracings from L-E photomicrographs were combined with groundmass measurements from TIMA panoramic images (Supplemental Fig. 7, Fig. 8). L-4B was not considered due to an insufficient phenocryst population count. We combined 733 groundmass measurements derived from XPL tracings with 64795 TIMA panoramic groundmass measurements. CSDSlice determined a best-fit aspect ratio of 1:0: 2.5: 4.5, 1: 2.2: 3.2, and 1.2: 2.0: 3.2 for the first 4000, second 4000 and third 4000 largest measurements, respectively. All R^2 were > 0.80 and provide agreement with actual crystal shape (Morgan and Jerram, 2006) regardless of the portion of the size population analyzed. Because

CSD corrections can only process 20001 entries at a time, 19268 groundmass measurements were used, providing a minimum major axis = 14.38 μm. Results from combining XPL-derived phenocrysts and TIMA-derived groundmass length measurements are shown in Figure 8. The increase in slope from coarser to finer size populations suggests a change in nucleation and crystal growth environments, roughly correlating to three major stages, labeled A, B, and C.

An initial inspection of the microlite population in thresholded images suggests that when "fill holes" are included for image analysis in ImageJ, the effects of truncating microlite borders are minimized, thus reducing bias in panoramic measurements of microlites (as opposed to phenocrysts). Figure 8 produces a ln(n^0) value (y-intercept) of 10.96 mm^{-4} when based on a regression slope of -14.1. This value is significantly larger than those indicated by the other methods in Table 4, suggesting that high-resolution TIMA images may potentially provide more robust upper boundaries of maximum nucleation population densities, if not more accurate nucleation densities than manual-phenocryst-tracing-plus-back-extrapolation would permit.

EBSD detection of fabric and discrete crystals in a complex cluster

Complex plagioclase twinning, especially as viewed in photomicrographs, can obscure visual detection of discrete-crystal boundaries within clusters. As such, twinning presents challenges to obtaining accurate crystal lengths with manual methods. To assess possible twinning-related issues with discrete crystal detection, we compared crystal counts from a single plagioclase-only cluster and surrounding groundmass from sample L-E using four types of images: 1) photomicrograph, 2) BSE, 3) TIMA-derived phase image, and 4) EBSD-derived orientation map (Fig. 9). Only crystals that were components of the all-plagioclase cluster were measured, and the surrounding groundmass ignored. BSE and TIMA phase images (Figs. 9B and 9C) only produce a single, contiguous particle although the cluster morphology suggests multiple crystals are present. EBSD and our MTEX script (Supplemental File 1) detected 51 discrete plagioclase crystals using a major axis length of an equal-area ellipse > 150 μm, but only ~40 crystals could be visually identified in the cluster image (Fig. 9D) whereas only 27 could be manually detected from the photomicrograph (Fig. 9A). Our MTEX script more frequently defined and detected individual crystals than manual methods. This difference becomes significant with cluster-rich samples, as an average of three unidentified discrete phenocrysts across multiple clusters within a sample will variably affect CSDs, provided the script accurately defines intra-crystal twinning patterns.

In addition to crystal lengths, EBSD orientation maps yield information on preferred orientations of plagioclase phenocrysts and groundmass populations as well as twin types. Our script determined the following twin types (Fig. 9D): 29% albite, 12% Carlsbad, 17% albite-Carlsbad, 1.3% pericline and <1% other. The script also produced a qualitative fabric analysis using EBSD M-indices; a groundmass M-index of 0.0150 and a phenocryst M-index of 0.0891 suggests mild orientation for the phenocryst population and less preferred orientation for the groundmass population, so neither fabric is completely random. M-indices suggest agreement with assumptions of random microlite orientation for CSD analysis using CSDSlice and CSDCorrections. The groundmass M-index here, however, only represents a local occurrence on a thin-section scale, and caution should be taken in assuming any large-scale effects. In the case of the cluster from sample L-E, vesicle areas were purposely avoided because plagioclase microlite alignment was noticed along vesicle walls. Increased vesicle presence may correlate to localized plagioclase alignment and so highly vesiculated samples may require a more thorough orientation analysis.

DISCUSSION

Texture and image type can create differences in apparent crystal lengths. These differences were evident in the plagioclase $L \geq 150$ μm population where manual tracing could isolate discrete crystals regardless of fracturing and clustering effects, but automated SEM-based methods could only detect discrete crystals based on immediately surrounding gaps of non-plagioclase compositions. Although BSE images frequently serve as a base image from which crystal lengths are manually marked, this is only feasible when crystal contiguity is minimal, and so cluster-free textures would produce appropriate working BSE images. Manual methods, however time-consuming, still provide the most accurate assessment of crystal length regardless of texture. Given that plagioclase is commonly twinned and zoned in magmatic samples, high resolution photomicrographs reflect optical properties that indicate demarcation boundaries between plagioclase crystals. These images can therefore more easily assist in visual detection of discrete crystals.

In assessing the feasibility of automated mineralogy imaging for extracting crystal lengths, TIMA panoramic images (based on the opposing textures of bimodal L-4B and seriate L-E) created upward shifts in CSD curves compared to manual tracing methods. This does not necessarily imply that thresholding-and-length-determination in ImageJ with panoramic images is an entirely inferior method to manual tracing in photomicrographs; on the contrary, although results show a systematic CSD curve shift, TIMA images may serve to mark upper boundaries of nucleation densities (Fig. 7). There are also human operator issues to consider, such as confidence in the user actually having isolated all crystals $L \geq 150$ µm in any given sample. Quality control issues likely vary across research, and this is why automated methods have the potential to serve as an additional quality control check on more traditional manual approaches. Does the use of a digital stylus, mouse, or trackball present bias in obtaining accurate crystal outlines due to limitations on the movement resolution (dots-per-inch, or DPI) of each device? There is no consistency across research other than basic methodological approaches (e.g. threshold an image, outline, process in ImageJ, extract lengths), and often methodological assumptions must be made by the reader since exhaustive details are typically not provided.

We noted fundamental differences in two types of automated imaging approaches, EDS and EBSD. While automated mineralogy focuses on elemental mapping, EBSD focuses on crystal orientation that involves addressing zero-data pixels with a noise-reduction process. The later approach addresses the problem of length acquisition from grainy textures and missing pixels (common in our plagioclase EDS maps) by emphasizing crystal orientation and zero-pixel infilling. Therefore, from an EBSD image, one determines both fabric and potentially length from completely pixeled crystals. Although it was beyond the scope of this study to focus on EBSD images for crystal length measurements, we find this type of image acquisition to be superior to others in terms of providing both fabric information and crystal length. We noted that in both samples, phenocrysts were variably fractured, sieved, and oriented and so the TIMA software would have provided inconsistent measurements regardless of its ability to calculate length based on a diameter of an equal-area circle. ImageJ could not correctly identify discrete phenocrysts for each sample using a single filling-in protocol with thresholded EDS images, although ImageJ's use of bounding ellipses circumvented the effects of missing pixels.

Manual tracing provided the only successful method for reliably identifying discrete plagioclase crystals. In terms of producing CSDs that reflect either crystals isolated from clusters versus clusters still intact, two textural factors provided insight: 1) discontiguity and 2) post-adhesion zoning patterns. In most clusters, either detectable discontiguity was present and/or a predominant non-shared crystal surface existed (Fig. 2B, for example). In these cases, length measurements from isolated discrete crystals should produce accurate CSDs. However, the cluster in Figure 9 suggests post-adhesion zoning, possibly due to synneusis. The lower half of Figure 9A (photomicrograph) shows a longer northwest aligned plagioclase crystal. However, the same area in Figure 9D (EBSD) shows a different outline pattern of the same crystal. In these cases, combining the EBSD orientation-based crystal outline with additional zoning patterns indicates that the lower half of this cluster experienced post-adhesion crystal growth. If this type of cluster were dominant, CSDs determined from isolated crystals would reflect a different growth rate, as length measurements would reflect growth on a restricted portion of the crystal surfaces. Cluster analysis that combines EBSD images and photomicrographs (or BSE images properly thresholded) has the potential to identify cluster styles which may reflect CSDs with more than one growth rate.

As fabric has an obvious effect on apparent crystal lengths, a quantitative approach to fabric assessment should exist for all CSD analyses. When EBSD analysis is cost prohibitive, orthogonal cut sections (preferably three) should serve as a minimum requirement. Although obtaining accurate CSDs was not the goal of the orthogonal cut analysis, comparing CSD curvature and curve placement for fabric detection was: if contiguity, clustering and other texturally controlled effects were present to the same extent in both sections, the sections should theoretically produce similar CSDs. Within each cut section (L-4B and V4) the three sampled groundmass regions are virtually identical for L-4B (Fig, 4A and 4C) but diverge slightly for V4 (Fig 4B and 4D) at $L > \sim 10$ µm, presumably due to insufficient crystal counts. Direct comparison of the two orthogonal sections against each other (Fig. 5C; the three sampled regions within each cut-section are treated as single area) suggests that cut section L-4B has a slightly greater population density but a narrower size range than V4. The increased size range of V4 may be due in part to increased contiguity, which has the effect of depressing the population densities of smaller size crystals, but if contiguity is assumed similar between cut sections, then variations in CSDs are real despite the proximity of sampled areas. Furthermore, we avoided regions with vesicles for both EBSD and BSE orthogonal cut section analyses given plagioclase preferred orientation was noted along some vesicle walls. Highly vesiculated samples may exert an orientation bias that skews aspect ratio and length determination.

A significant contribution to CSD analysis from our work rests on high-resolution automated SEM-based approaches, both EDS and EBSD. In the case of groundmass plagioclase (L <150 µm), a high-resolution 2 µm SEM scan permits refinement of the groundmass size population into multiple groups, each with its own aspect ratio, for analysis of late-stage eruptive behavior. The above approach produced an asymptotic-like CSD curve for L-E as the groundmass size population was continuously refined (Fig. 8).

Strongly bimodal L-4B displayed a sharper increase in CSD slope at L = ~1.5 mm versus a more continuous curve for highly seriate L-E (Fig. 7). Although a sudden slope change is expected in highly bimodal samples, greater negative slopes at L < 150 μm for L-4B suggest a relatively faster late-stage eruption versus that suggested by L-E. Coupled with the on-vent location of bimodal L-4B and its occurrence during the first half of the Laki eruptions, the relative lack of phenocrysts does not provide a robust account of continuous phenocryst nucleation-and-growth suggested by late-stage L-E. Relatedly, if phenocrysts from L-4B share nucleation-and-growth origins with phenocrysts from L-E, it is not clear along which discrete portions of a continuous nucleation-and-growth CSD curve these phenocrysts originated or are significantly related to.

Although regions A, B, and C in Figure 8 represent crystal populations large enough to produce a robust CSD, each region is representative of unique textural challenges. Region A considers plagioclase length measurements that Castro et al. (2003) consider problematic due to cut-section lengths smaller than the standard thickness of the thin section (30 μm) while region B represents groundmass size populations calculated from plagioclase length measurements approximately greater than the thickness of the thin section. Contiguity and fracturing effects are directly correctable through manual tracing for region C crystals and progressively more difficult for crystals within region B and A. Aspect ratio evolution along a CSD curve for a seriate texture should consider multiple size populations and therefore potentially multiple aspect ratios. Aspect ratio evolution for seriate L-E through all three regions (Fig. 8) reflected increasingly compact and less faceted forms with decreasing size populations. Within region C, aspect ratios showed variations in intermediate and long axes lengths depending on what portion of the largest size phenocryst populations were considered. Figure 5 suggests that such variations in aspect ratios have the potential to produce different CSDs.

EBSD data processed with the MTEXT toolbox detected 1345 discrete plagioclase crystals in the area shown in Figure 9D. With a TIMA-based image, over 6000 particles were detected, and this result may have been due to a combination of fracturing and a slightly finer scan resolution. Noise correction in ImageJ using the “despeckle” function four times eventually produced ~1390 particles over a similar area but also introduced increased particle contiguity.

The effects of cut sections through swallowtail groundmass populations were not examined. Swallowtail cut sections should theoretically contribute to the smaller groundmass size populations, but the count may be offset by the fact that swallowtail termination cut-sections are smaller than the thickness of the thin-section (the intersection-probability effect). Although approaches have been devised that model random cuts through simple solids (Morgan and Jerram, 2006), more complicated forms have not been similarly analyzed. 3D numeric modeling of random cuts through dendritic shapes is required.

IMPLICATIONS

Our observations suggest that internal consistency only holds when all samples are texturally similar so that a single method does not negatively exploit any texture-based effects on obtaining crystal lengths. Preserving internal consistency does permit reliable intra-study comparisons between samples, but internal consistency does not translate to consistency across research groups. The end goal is that CSD analyses across research groups should reflect consistent and reproduceable results. Even the assumption of a random fabric by only a visual estimation is inadequate, and here we demonstrate that the use of orthogonal BSE images may be sufficient in lieu of costlier EBSD analysis. Provided that our MTEX script correctly adjusted for intra-cluster twinning, we found that local variations in fabric likely occur and that clusters may contain a greater number of discrete crystals than even visual estimations from photomicrographs permit. A coarser scan resolution addressing discrete crystal occurrence in multiple clusters would have been more appropriate and a direction for future work.

Manual approaches for obtaining phenocryst lengths remain more reliable than automated methods, and a fully automated approach is not currently feasible. However, high-resolution automated SEM-based approaches in general do offer the opportunity to investigate late-stage eruptive behavior through groundmass analysis, although anhedral forms and their corresponding aspect ratios require refinement through voxel modeling (i.e. swallowtail forms). Automated mineralogy may provide cross-research consistency in results for groundmass analyses, highlighting manual-based bias (again, if textural similarities hold). Table 4 suggests that automated mineralogy images may produce results similar to manual tracing when more seriate textures are considered.

Although plagioclase growth rates of ~10^{-10} mm s^{-1} are typical (Cashman, 1990) and often used to calculate residence times from CSDs (Brugger and Hammer, 2010 and references therein), growth rates as high as 10^{-6} mm s^{-1} for microlite growth during decompression have been reported (Hammer et al., 1999). Actual growth rates should not only vary immediately pre-, syn-, and post-eruption, but they should vary during phenocryst formation as well. Therefore, CSDs should be considered in the context of multiple growth rates and aspect ratios. However, we have never observed the application of multiple growth rates for interpreting a single CSD curve that would reflect real-world, evolving crystallization environments.

ACKNOWLEDGEMENTS

The authors are very grateful to Marian Holness of the University of Cambridge's Department of Earth Sciences as well as to an anonymous reviewer for exceptionally critical and thoughtful feedback that led to a greatly improved final manuscript. We also thank Wendy Harrison from the Colorado School of Mines for editing suggestions on the original draft of this manuscript; Kevin Mahan's group in Geological Sciences at the University of Colorado at Boulder for remote use of their EBSD software; and Tyler C. Brown at the University of Wyoming's Materials Characterization Laboratory for his assistance with EBSD analysis, sample preparation, and Oxford Channel 5 software training.

Endnote:

This publication uses data collected within the framework of the following: Cone, K.A. (2018) Refining crystal size distributions and kinetic histories using automated scanning electron microscopy and manual methods: A hybrid approach, 91 p. M.S. thesis, Colorado School of Mines, Golden.

REFERENCES

Bindeman, I., Sigmarsson, O., and Eiler, J. (2006) Time constraints on the origin of large volume basalts derived from O-isotopes and trace element mineral zoning and U-series disequilibria in the Laki and Grímsvötn volcanic system. Earth and Planetary Science Letter, 245, 245-259.

Brugger, C.R., and Hammer, J.E. (2010) Crystal size distribution analysis of plagioclase in experimentally decompressed hydrous rhyodacite magma. Earth and Planetary Letters, 300, 246-254.

Brugger, C.R., and Hammer, J.E. (2015) Prevalence of growth twins among anhedral plagioclase microlites. American Mineralogist, 100, 385-395.

Cashman, K.V., and Marsh, B.D. (1988) Crystal size distribution (CSD) in rocks and the kinetics and dynamics of crystallization II: Makaopuhi lava lake. Contributions to Mineralogy and Petrology, 99, 292-305.

Cashman, K.V. (1993) Relationship between plagioclase crystallization and cooling rate in basaltic melts. Contributions to Mineralogy and Petrology, 113, 126-142.

Castro, J.M., Cashman, K.V., and Manga, M. (2003) A technique for measuring 3D crystal size distributions of prismatic microlites in obsidian. American Mineralogist, 88, 1230-1240.

Cone, K.A. (2018) Refining crystal size distributions and kinetic histories using automated scanning electron microscopy and manual methods: A hybrid approach, 91 p. M.S. thesis, Colorado School of Mines, Golden.

Gottlieb, P., Wilkie, G., Sutherland, D., Ho-tun, E. Suthers, S., Perera, K., Jenkins, B., Spencer, S., Butcher, A.R., and Rayner, J. (2000) Using quantitative electron microscopy for process mineralogy applications. Journal of the Minerals, Metals and Materials Society, 52, 24-25.

Gu, Y. (2003) Automated Scanning Electron Microscope Based Mineral Liberation Analysis – An Introduction to JKMRC/FEI Mineral Liberation Analyser. Journal of Minerals and Materials Characterization and Engineering, 2, 33-41.

Guilbaud, M.N., Blake, S., Thordarson, T., and Self, S. (2007) Role of syn-eruptive cooling and degassing on textures of lavas from the AD 1783-1784 Laki eruption, south Iceland. Journal of Petrology, 48, 1265-1294.

Hammer, J.E., Cashman, K.V., Hoblitt, R.P., and Newman, S., (1999) Degassing and microlite crystallization during pre-climactic events of the 1991 eruption of Mt. Pinatubo, Philippines. Bulletin of Volcanology. 60, 355-380.

Higgins, M. (2000) Measurement of crystal size distributions. American Mineralogist, 85, 1105-1116.

Higgins, M. (2006) Quantitative Textural Measurements in Igneous and Metamorphic Petrology. Cambridge University Press, Cambridge, 276 pp.

Holness, M.B. (2014). The effect of crystallization time on plagioclase grain shape in dolerites. Contributions to Mineralogy and Petrology, 168, 1076.

Hrstka, T, Gottlieb, P., Skála, R., Breiter, K., and Motl, D. (2018) Automated mineralogy and petrology – applications of TESCAN Integrated Mineral Analyzer (TIMA). Journal of Geosciences, 63, 47-63.

Kirkpatrick, R.J. (1977) Nucleation and growth of plagioclase, Makaopuhi and Alae lava lakes, Kilauea volcano, Hawaii. Geological Society of America Bulletin, 88, 78-84.

Launeau, P., and Robin, P.F. (2015) Determination of fabric and strain ellipsoids from measured sectional ellipses – implementation and applications. Journal of Structural Geology, 27, 2223-2233.

Mainprice, D., Bachmann, F., Hielscher, R., and Schaeben, H. (2015) Descriptive tools for the analysis of texture projects with large datasets using MTEX: strength, symmetry and components. Geological Society of London, Special Publications, 409, 251-271.

Marsh, B.D. (1988) Crystal size distribution (CSD) in rocks and the kinetics and dynamics of crystallization I: Theory. Contributions to Mineralogy and Petrology, 99, 277-291.

Marsh, B.D. (1998) On the interpretation of crystal size distributions in magmatic systems. Journal of Petrology, 39, 553-599.

Meurer, W.P., and Boudreau, A.E. (1998) Compaction of igneous cumulates, part II: Compaction and the development of igneous foliations. Journal of Geology, 106, 293-304.

Mock, A., and Jerram, D.A. (2005) Crystal size distributions (CSD) in three dimensions: Insights from the 3-D reconstruction of a highly porphyritic rhyolite. Journal of Petrology, 46, 1525-1541.

Morgan, D.J., and Jerram, D.A. (2006) On estimating crystal shape for crystal size distribution analysis. Journal of Volcanology and Geothermal Research, 154, 1-7.

Neave, D., Buisman, I., and Maclennan, J. (2017) Continuous mush disaggregation during the long-lasting Laki fissure eruption, Iceland. American Mineralogist, 112, 2007-2021.

Neave, D., Passmore, E., Maclennan, J., Fitton, G., and Thordarson, T. (2013) Crystal-melt relationships and the record of deep mixing and crystallization in the AD 1783 Laki eruption, Iceland. Journal of Petrology, 54, 1661-1690.

Orlando, A., D'Orazio, M., Armienti, P., and Borrini, D. (2008) Experimental determination of plagioclase and clinopyroxene crystal growth rates in the anhydrous trachybasalt from Mt. Etna (Italy). European Jornal of Mineralogy, 20, 653-664.

Passmore, E., Maclennan, J., Fitton, G., and Thordarson, T. (2012) Mush disaggregation in basaltic magma chambers: evidence from the ad 1783 Laki eruption. Journal of Petrology, 53, 2593-2623.

Prior, D., Boyle, A.P., Brenker, F., Cheadle, M.C., Day, A., Lopez, G., Peruzzo, L., Potts, G.J., Reddy, S., Spiess, R., Timms, N., Trimby, P., Wheeler, J., and Zetterström, L. (1999). The application of backscatter diffraction and orientation contrast imaging in the SEM to textural problems in rocks. American Mineralogist, 84, 1741-1759.

Randolph, A.D., and Larson, M.A. (1971) Theory of particulate processes. Academic Press, New York, 251 pp.

Schneider, C. A., Rasband, W.S., and Eliceiri, K. W. (2012) NIH Image to ImageJ: 25 years of image analysis. Nature Methods, 9, 671-675.

Shea, T. and Hammer, J.E. (2013) Kinetics of cooling- and decompression-induced crystallization in hydrous mafic-intermediate magmas. Journal of Volcanology and Geothermal Research, 260, 127-145.

Skemer, P., Katayama, I., Jiang, Z., and Karato, S. (2005) The misorientation index: Development of a new method for calculating the strength of lattice-preferred orientation. Tectonophysics, 411, 157-167.

Sutherland, D. (2007) Estimation of mineral grain size using automated mineralogy. Minerals Engineering, 20, 452-460.

Thordarson, T., and Self, S. (1993) The Laki (Skaftár Fires) and Grímsvötn eruptions in 1783-1785. Bulletin of Volcanology, 55, 233-263.

Xu, C., Zhao, S-R., Li, C., and He, X. (2016) Plagioclase twins in a basalt: an electron backscatter diffraction study. Journal of Applied Crystallography, 49, 2145-2154.

FIGURE CAPTIONS

Figure 1. Iceland (smaller inset image, upper left) and the Laki flows (right). Black areas in the inset figure represent the Neovolcanic Zone which comprises three tectonically and volcanically active belts initially formed in early Cenozoic; the Zone includes the Eastern Volcanic Zone (2), Western Volcanic Zone (1), and the Northern Volcanic Zone (3) (see inset figure). The shaded red box in the inset represents the area shown in Figure 2 where the two samples were collected. The red dashed circle indicates the approximate region of the underlying mantle plume, derived from Thordarson and Höskuldsson (2008). The orange triangle represents Grímsvötn (Laki Mountain). Internal white areas represent glaciers. The general outline of Iceland and the Neovolcanic Zone locations are modified from Passmore et al. (2012).

Figure 2. Discrete crystals within crystal clusters in Sample L-4B, cross polarized light. Image A shows typical all-cpx clusters as well as isolated cpx crystals (center-left, twinned). Image B shows the common occurrence of pl+cpx clusters. The cluster on the right shows elongated plagioclase with indistinct boundaries. Image C shows an all-plagioclase glomerocryst from sample L-4B, cross polarized light. Note the strong degree of optical continuity as suggested by shared extinction behavior. This continuity suggests that the individual crystals within the cluster are similarly oriented.

Figure 3. Discrete crystals and crystal cluster types in sample L-E, cross polarized light. Crystal cluster types are similar to those of L-4B. Note in D the pronounced internal sieving of the discrete plagioclase phenocryst, suggesting disequilibrium conditions. A and B show discrete

and cluster styles of plagioclase, respectively. C shows a slight variation of pl+cpx clustering, where plagioclase microlites are highly elongate.

Figure 4. Groundmass-only CSD curves generated from BSE images for orthogonal sets of proximal pairs: L-4B 1 is orthogonal and proximal to V4 1, L-4B 2 to V4 2, and L-4B 3 to V4 3. Two aspect ratios representing two slightly different shapes (1:4:8 = prismatic = Figures A and B; 1:8:8 = tabular = Figs. C and D) still produce strong correlations within samples. NE (non-edge) represents BSE analyses that ignore particles that border image edges. E represents BSE analyses where edge-bordering particles were included. Figures A and C (left column) show strong correlations in CSD curve patterns, suggesting similarity in orientation patterns and in contiguity styles of groundmass plagioclase. Divergence occurs at the larger sizes. Floating points at the largest sizes are due to bin counts < 3. Five bins per decade were used.

Figure 5. Comparisons between L-4B and V4 groundmass plagioclase, emphasizing aspect ratio effects from non edge-bordering and edge-bordering BSE image processing in ImageJ. Figures A and B compare the effects of tabular (1:8:8) and prismatic (1:4:8) shapes. Including edge-bordering particles creates flatter curves at the larger L values (Figs. A and B triangular points). Irregularities are likely due to small sample sizes for larger L values. However, trends are similar within each aspect ratio. Figure C shows that L-4B produces greater nucleation population densities than V4. Curve shapes are still similar and differences between 1:4:8 and 1:8:8 curves are strictly due to aspect ratio choice.

Figure 6. Combined results for L-4B and V4 (composite) for a single aspect ratio (1:8:8)

reflecting a tabular form with non edge-bordering analysis in ImageJ. C represents the average particle size in μm. Random orientation of tabular plagioclase microlites is assumed for analysis. The V4+L-4B curve (red curve) shows the combined results in CSDCorrections using the three sampled areas for L-4B and the three sampled areas for V4.

Figure 7. A comparison of CSDs from L-4B and L-E. Length measurements for plagioclase phenocrysts were derived from manual tracings of photomicrographs and from panoramas and isolated-particle images. Four bins per decade were used for Figure A and 5 bins per decade for Figure B. *New aspect ratio* represents the use of the photomicrograph aspect ratio. The turndowns at the smallest L-values are likely due to an insufficient crystal count for the smallest L-value bins. Figure A shows an insufficient number of the largest phenocrysts such that floating points result. Panorama-sourced measurements consistently create the largest nucleation population densities while isolated-particle images produce the lowest.

Figure 8. CSD using phenocrysts from a photomicrograph tracing of L-E and groundmass information from a TIMA panorama image and includes all plagioclase species (An_0 to An_{100}). The CSD curve reflects seven bins per decade. Red vertical error bars reflect counting statistics only. Region C represents phenocrysts while regions A and B represent two populations of groundmass roughly separated by the thickness of a standard thin section (30 μm). Increasing length-to-width aspect ratios generally correspond with increasing size populations.

Figure 9. A complex all-plagioclase glomerocryst with surrounding groundmass, from sample L-E. Figure A shows outlines for 27 discrete crystals visually determined from a

photomicrograph. B (BSE image) and C (panoramic image) show the central cluster as a single, contiguous particle. D (EBSD) shows a color orientation map where different colors represent different orientations of plagioclase, and discrete crystals are outlined. The offset in the lower right-corner of D reflects a mis-stich in adjacent field scans, but no crystal measurements with obtained with this image.

Supplemental Figure 1. The original billets from L-4B and L-E (the orientations of which are indicated by the blue plane in the top figure) were cut lengthwise down the center and opened and rotated 90° in the direction of the arrows, with the newly exposed faces (red surface in the bottom and top figure) serving as the new surfaces of orthogonally oriented V4 and V1, respectively.

Supplemental Figure 2. The red circles represent the six regions from which BSE images were produced. L-4B (upper image, carbon coated) and orthogonally oriented V4 (lower image, pre-carbon coated) were sampled for groundmass crystal lengths only (crystal lengths under 150 μm). Since V4 is produced from a mid-sectional cut along the elongated direction of the billet from L-4B, more proximal areas to regions chosen in L-4B are closer to the upper and lower regions of the elongated direction as shown in V4. Bright region at the bottom-right is due to increased thinness of sample in that area. Field of view is ~30mm across.

Supplemental Figure 3. ~300 μm x ~250 μm BSE images from L-4B (Group A). Supplemental Figure 2 shows the location of the sampled groundmass areas. Feldspars appear dark gray.

DOI: https://doi.org/10.2138/am-2020-7007

Microlite texture appears random with minimal porosity (Φ) regions chosen. Areas near vesicles were avoided. Lighter phases are olivine, clinopyroxene and opaques.

Supplemental Figure 4. ~300 μm x ~250 μm BSE images from V4 (Group B), orthogonal to L4B. The three regions are spatially close to group A groundmass areas sampled in Supplemental Figure 1 but represent a perpendicular cut section. Elongated dark gray shapes are plagioclase, similar to that in Supplemental Figure 3. Only plagioclase ≤150 μm based on the long axis measurement were considered here.

Supplemental Figure 5. An example of segmenting, or digitally clipping, a larger plagioclase cluster into smaller components. A particle from an isolated-particle image (left) is selected (center-left, in blue) and manually separated into smaller particles. The goal is to create discrete crystals for length measurements in ImageJ. The particle is then automatically placed back into the isolated-particle image (right) by size rank according to the diameter of a best-fit circle.

Supplemental Figure 6. L-4B TIMA panoramic SEM-EDS image (A). Plagioclase crystals that displayed scanning issues, missing pixels or excessive fracturing were manually traced and filled in (B) by comparing the image to the thin section photomicrograph/polarizing microscope image.

Supplemental Figure 7. L-E TIMA panoramic SEM-EDS image (A). Plagioclase crystals that displayed scanning issues, missing pixels or excessive fracturing were manually traced and filled in (B) by comparing the image to the thin section photomicrograph/polarizing microscope image.

TABLES

Table 1. Major characteristics of discrete-style (single crystal) phenocrysts. For sample L-E, rare, tabular occurrences of internally, strongly sieved plagioclase crystals occur.

Laki basalt phenocryst characteristics (Discrete)			
Sample	Phase	~Size (mm)	Shape
L-4B	pl	up to 0.70	subhedral to euhedral
	cpx	up to 0.15	euhedral, equant
	ol	up to 0.30	subhedral, equant to subequant
L-E	pl	up to 0.80	subhedral to euhedral
	cpx	up to 0.30	equant
	ol	up to 0.45	subhedral euhedral

Table 2. Major characteristics of cluster-style phenocrysts.

Laki basalt phenocryst characteristics (Cluster)			
Sample	**Style**	**~Size (mm)**	**Texture/Observations**
L-4B	pl-only	up to 2.0	sometimes continuous extinction; zoned and twinned
	cpx-only	up to .25	clusters of two to four crystals
	pl+cpx	up to 1.35	often sub-ophitic with smaller occurrences larger ones are discrete-discrete clusters
	pl+cpx+ol	up to 0.40	rare
L-E	pl-only	up to 3.5	microlite flow alignment around largest clusters (product of two joined discrete-clusters?)
	cpx-only	up to 0.40	up to three contiguous members
	pl+cpx	up to 2.0	often sub-ophitic; largest cluster contains largest cpx crystals, up to 1.1mm
	pl+cpx+ol	up to 0.90	rarely observed

This is a preprint, the final version is subject to change, of the American Mineralogist (MSA)
Cite as Authors (Year) Title. American Mineralogist, in press.
DOI: https://doi.org/10.2138/am-2020-7007

Table 3. TIMA results of isolated-particle image editing from multi-field (panorama) phase maps. Column C includes the removal of any particles consisting of fewer than four pixels, resulted from digital clipping. Column B includes mis-stitched and edge-bordering particles. Columns A, B and C are exclusive of each other. Min and Max size columns are derived from TIMA's default size bins and represent bins defined by the diameter of an equal-area circle.

Multi-field scan characteristics (panorama)							
Group A	**Min size bin (µm)**	**Max size bin (µm)**	**No. of fields**	**(A) No. of particles created**	**(B) No. of particles deleted**	**(C) No. of particles created and then deleted**	**Total number of particles after (A), (B), (C)**
L-4B	[2.2, 2.6)	[185, 217)	56	149	33	17	425508
L-E		[298, 349)	114	4163	661	531	419378

DOI: https://doi.org/10.2138/am-2020-7007

Table 4. Kinetic characteristics derived from the isolated-particle phase images, panoramas, and photomicrographs used to determine CSDs. C = average crystal size, J = nucleation rate and n^0 = nucleation density. Table values were determined as follows, based on an assumed crystal growth rate of $G = 10^{-10}$ mm/s: C was calculated using regression slopes from CSDCorrections (m), where $C = -1/m$; n^0 was determined from directly from CSD corrections; $J = \exp(\ln(n^0)) * G$; and τ is defined as $C/G/(3.154*10^7)$. S: I: L = short: intermediate: long.

CSD characteristics by image ($L \geq 150$ µm)

DOI: https://doi.org/10.2138/am-2020-7007

Method	**Slope**		**ln (n^0)(mm^{-4})**		***C* (mm)**		**mean τ (days)**		***J* (mm-3 s^{-1})**		**Aspect ratio (S: I: L)**	
	L-4B	L-E	L-4B	L-E	L-4B	L-E	L-4B	L-E	L-4B	L-E	L-4B	L-E
Isolated particle	-5.01	-4.91	3.90	5.75	0.345	0.538	39896	62269	4.94E-09	3.14E-08	1.0: 3.0: 6.0	1.0: 2.1: 5.5
Panorama	-8.58	-6.51	7.04	7.62	0.296	0.324	34213	37500	1.14E-07	2.04E-07	1.0: 2.5: 5.5	1.0: 2.5: 5.0
Manual tracing	-5.62	-6.26	5.51	6.50	0.274	0.339	31713	39236	2.47E-08	6.65E-08	1.0: 3.6: 7.0	1.0: 2.5: 5.0

FIGURES

Figure 1

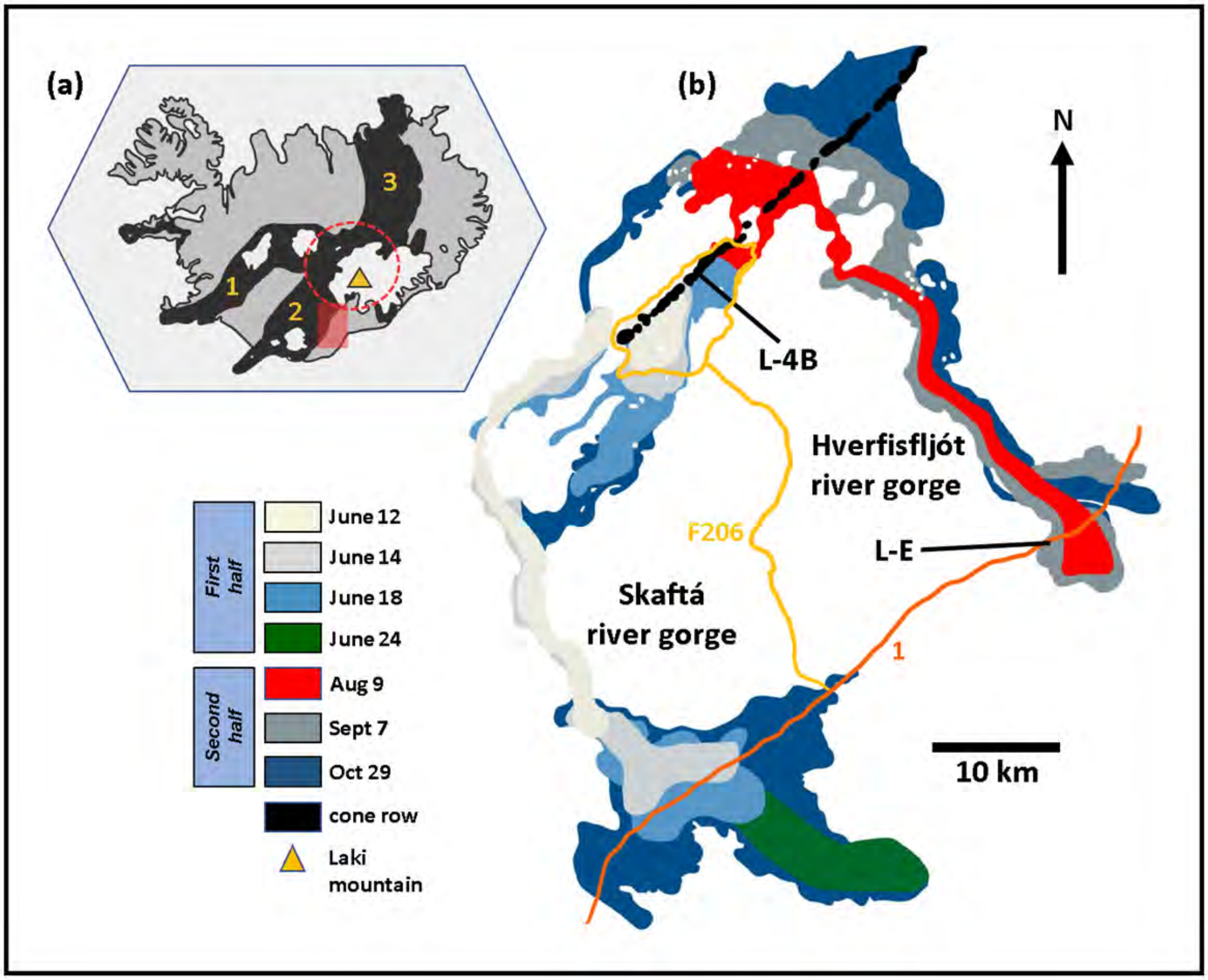

Figure 2

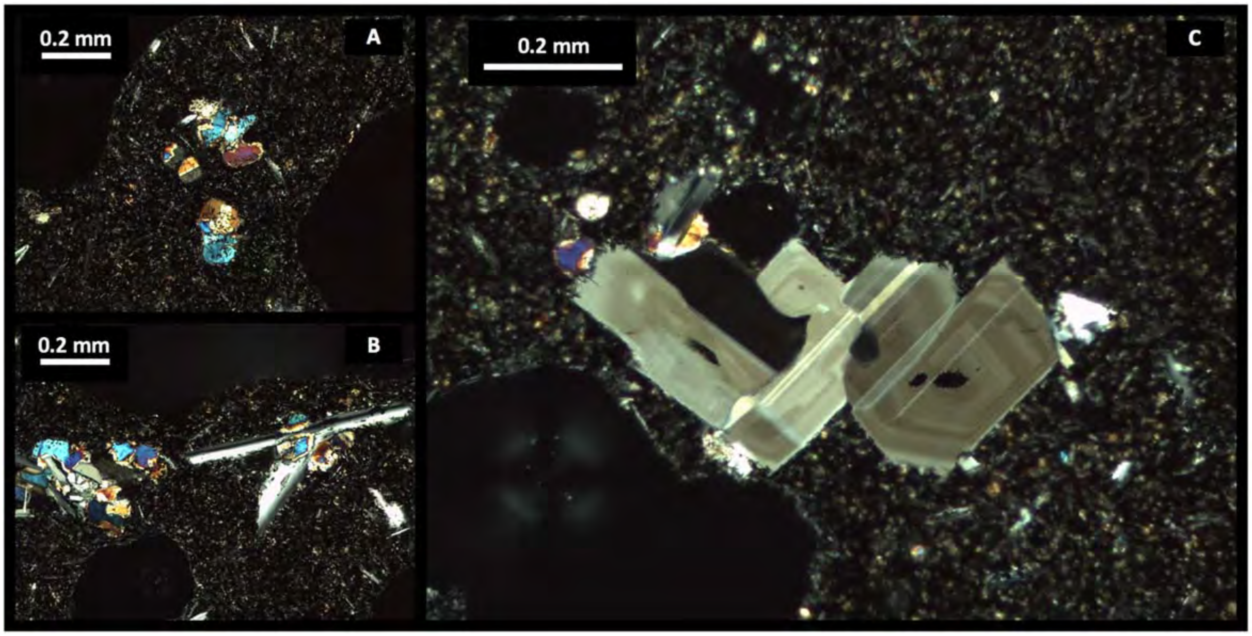

DOI: https://doi.org/10.2138/am-2020-7007

Figure 3

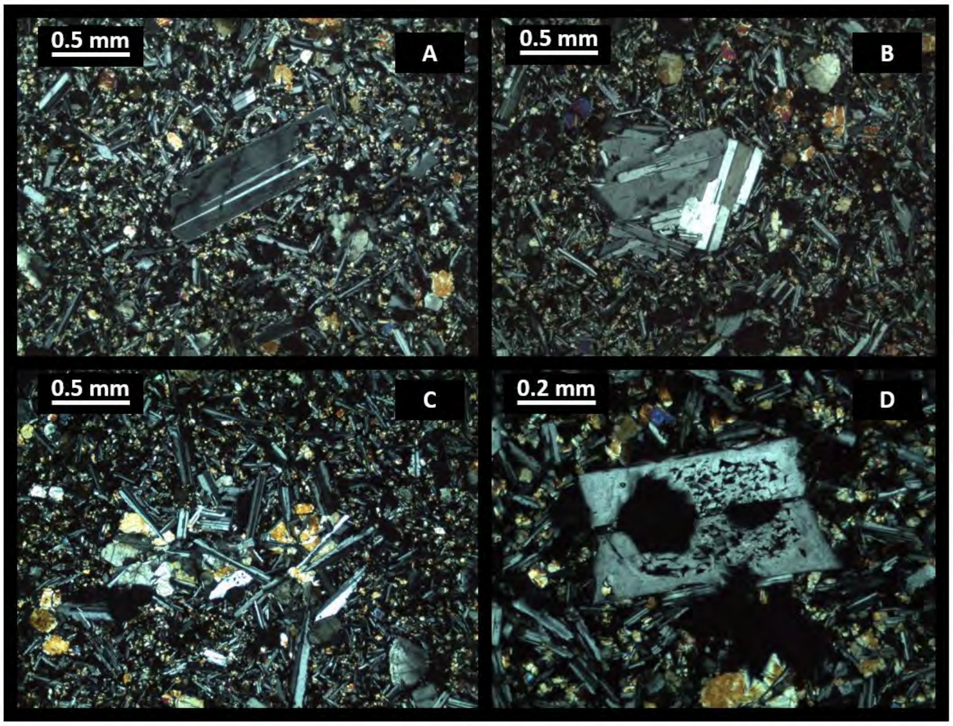

DOI: https://doi.org/10.2138/am-2020-7007

Supplemental Figure 1

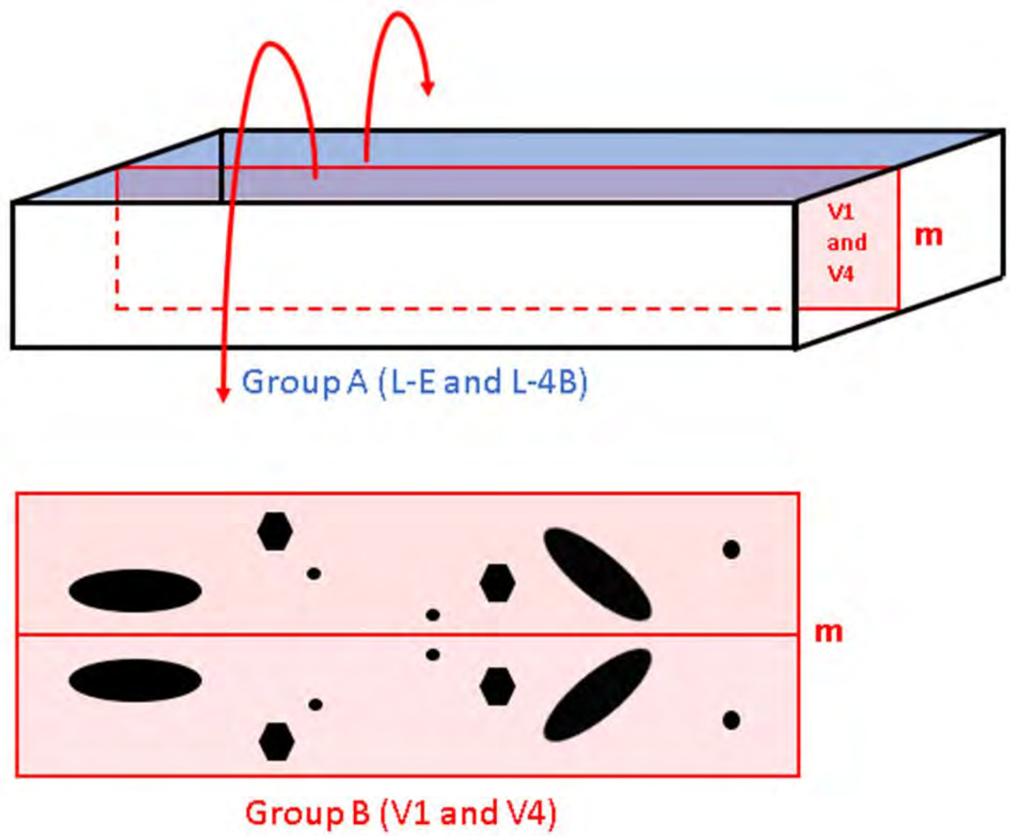

DOI: https://doi.org/10.2138/am-2020-7007

Supplemental Figure 2

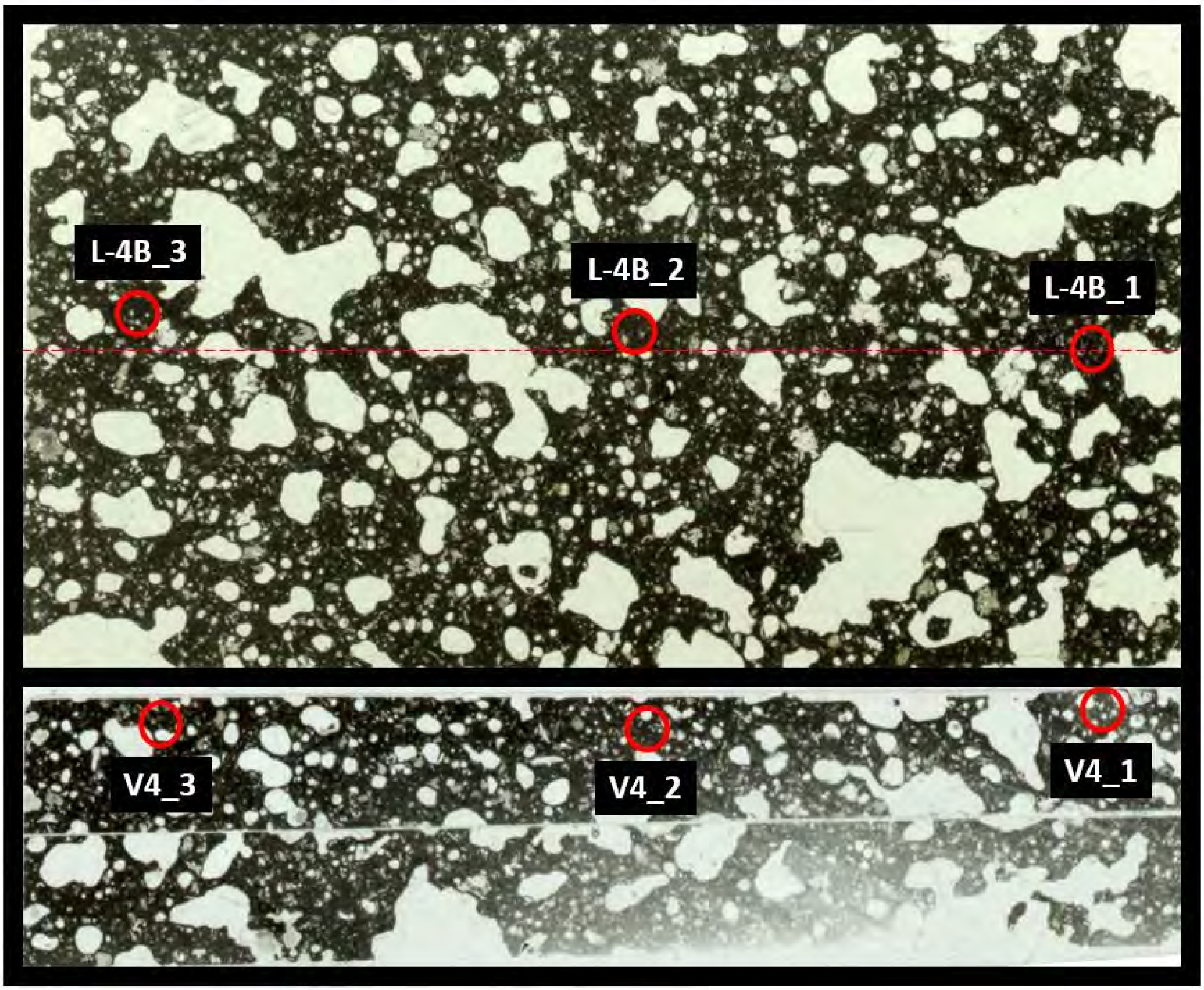

Supplemental Figure 3

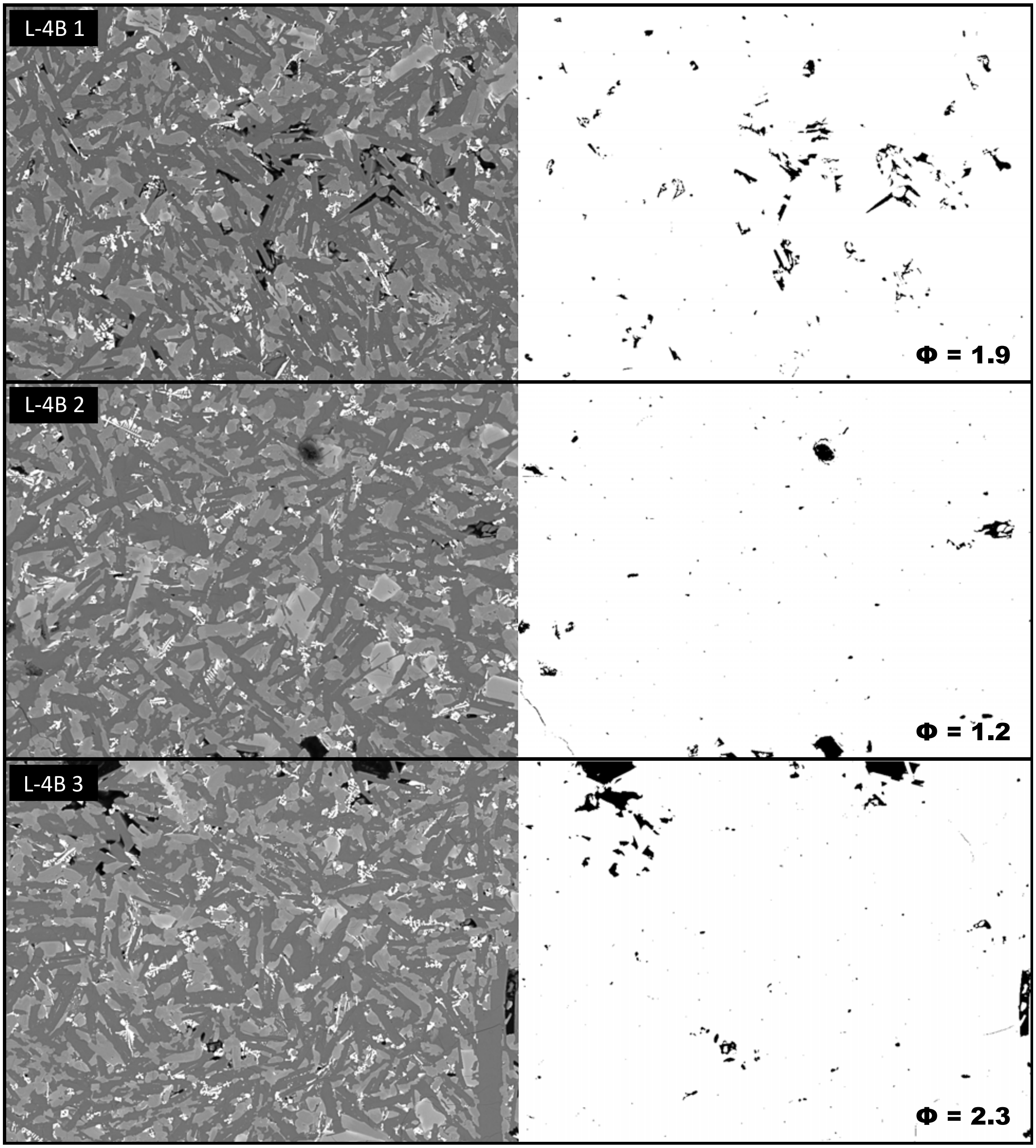

Supplemental Figure 4

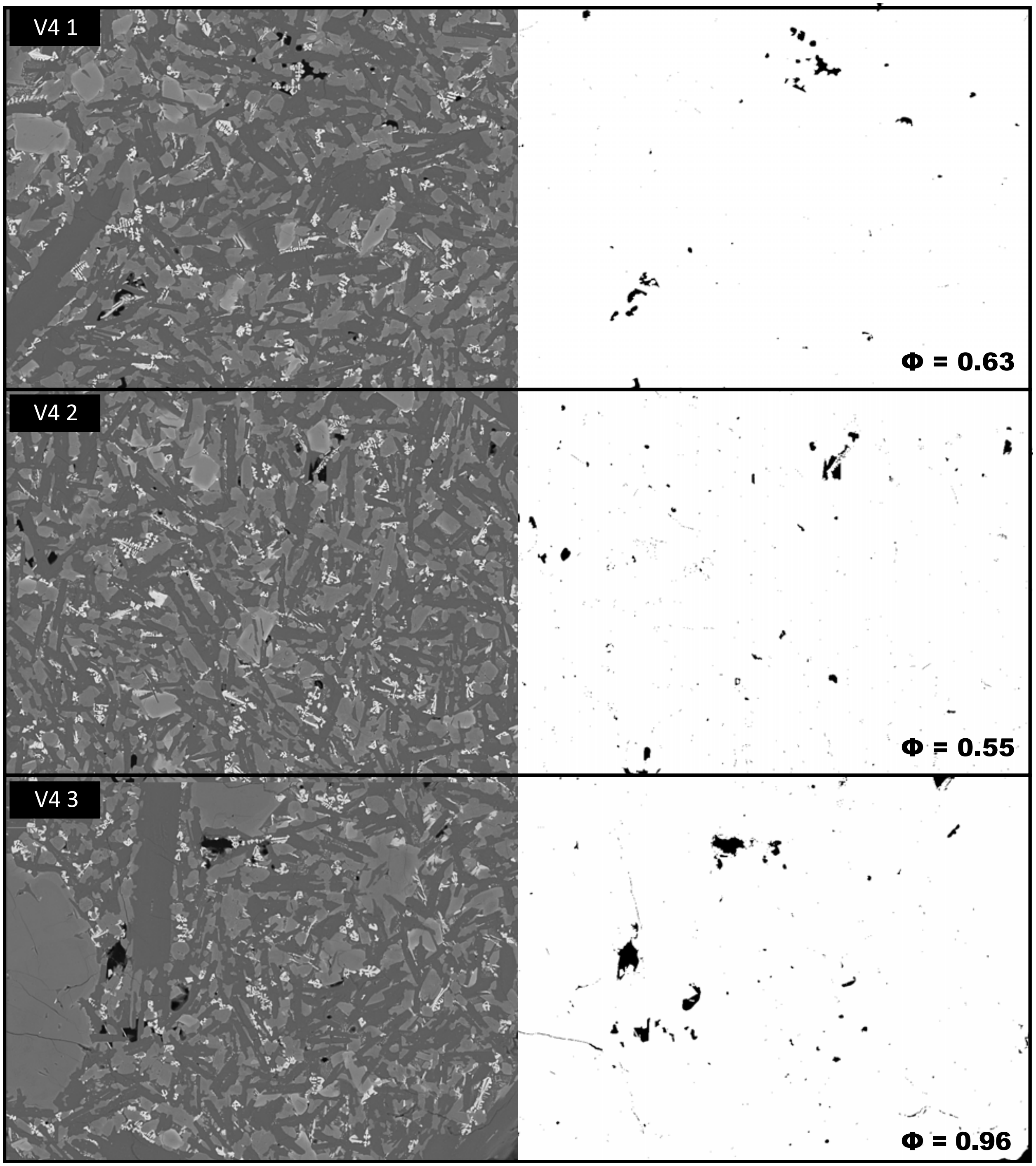

DOI: https://doi.org/10.2138/am-2020-7007

Supplemental Figure 5

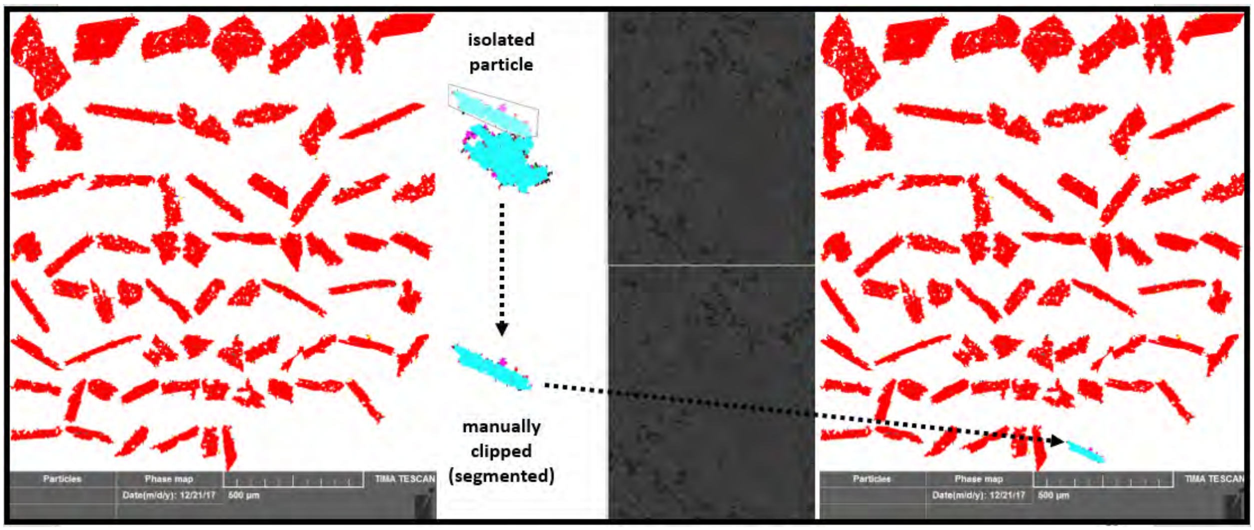

Supplemental Figure 6

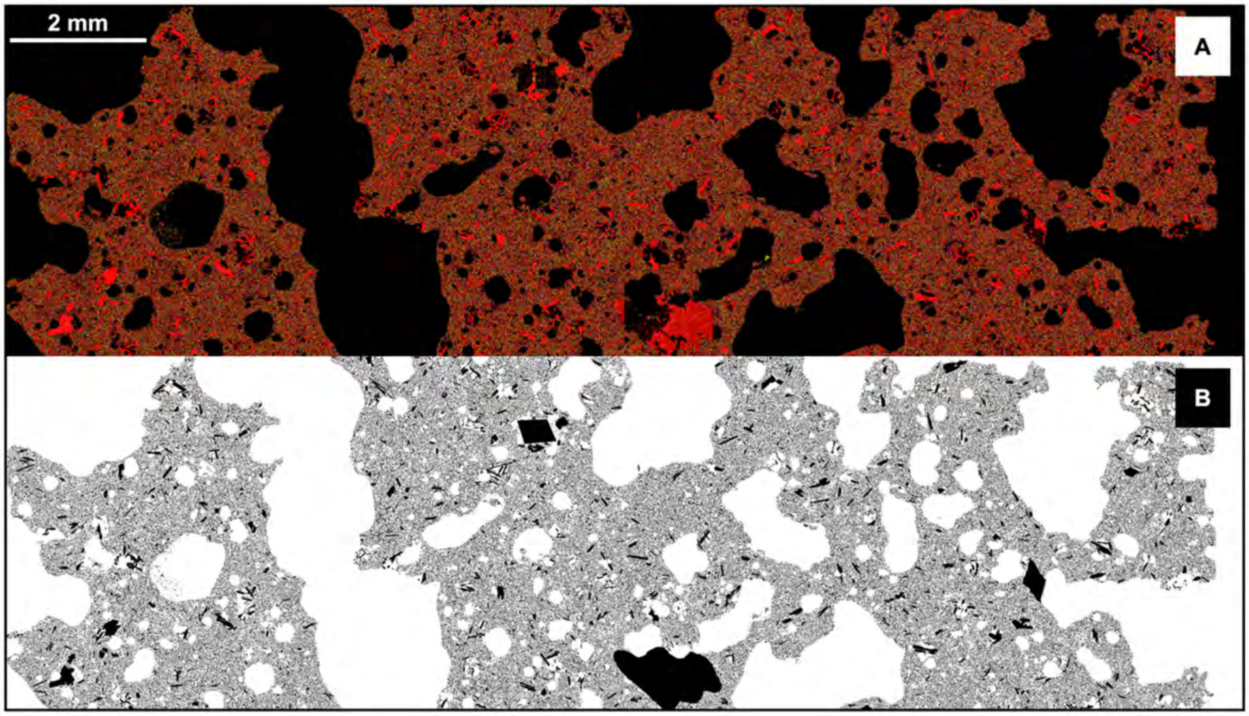

This is a preprint, the final version is subject to change, of the American Mineralogist (MSA)
Cite as Authors (Year) Title. American Mineralogist, in press.
DOI: https://doi.org/10.2138/am-2020-7007

Supplemental Figure 7

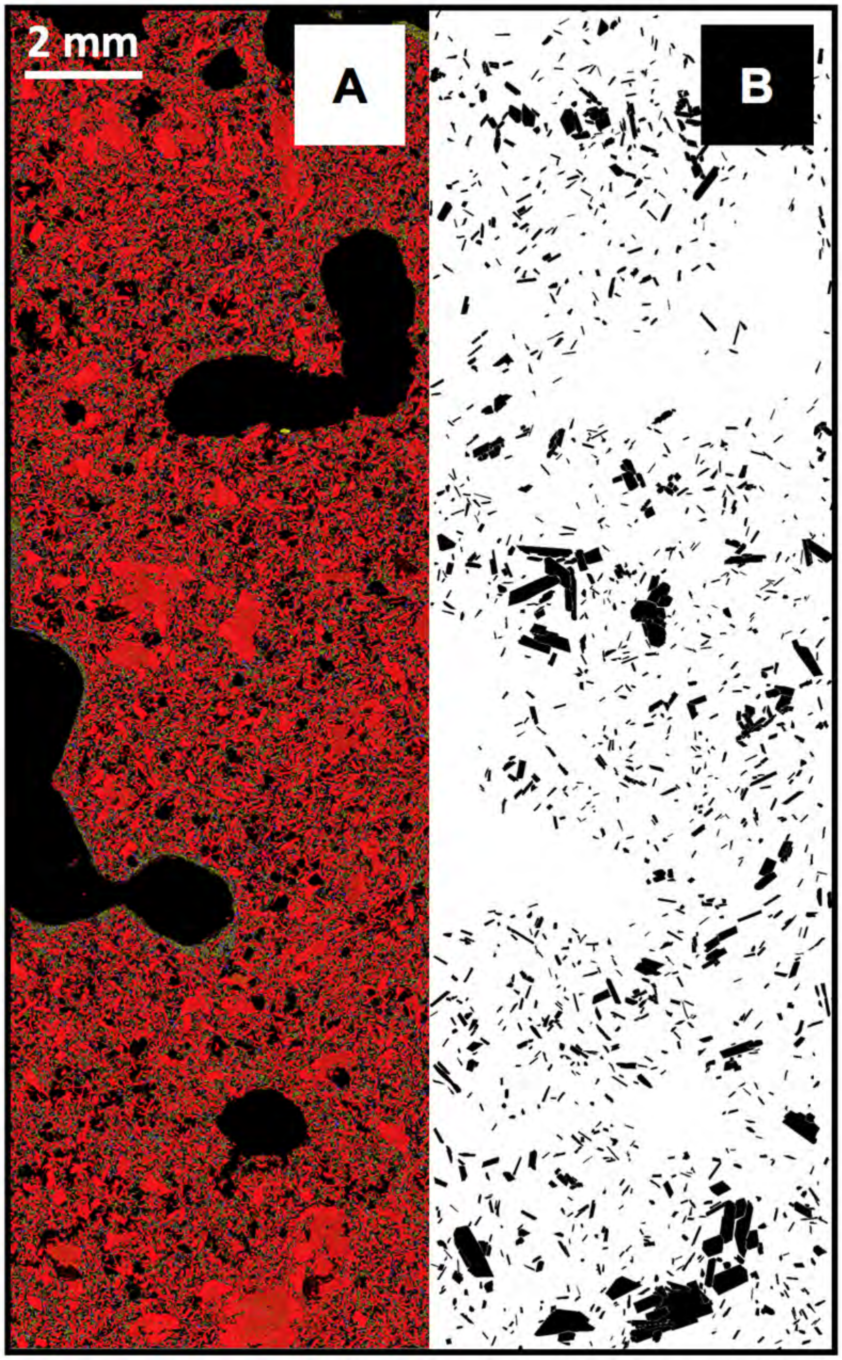

This is a preprint, the final version is subject to change, of the American Mineralogist (MSA)
Cite as Authors (Year) Title. American Mineralogist, in press.
DOI: https://doi.org/10.2138/am-2020-7007

Figure 4

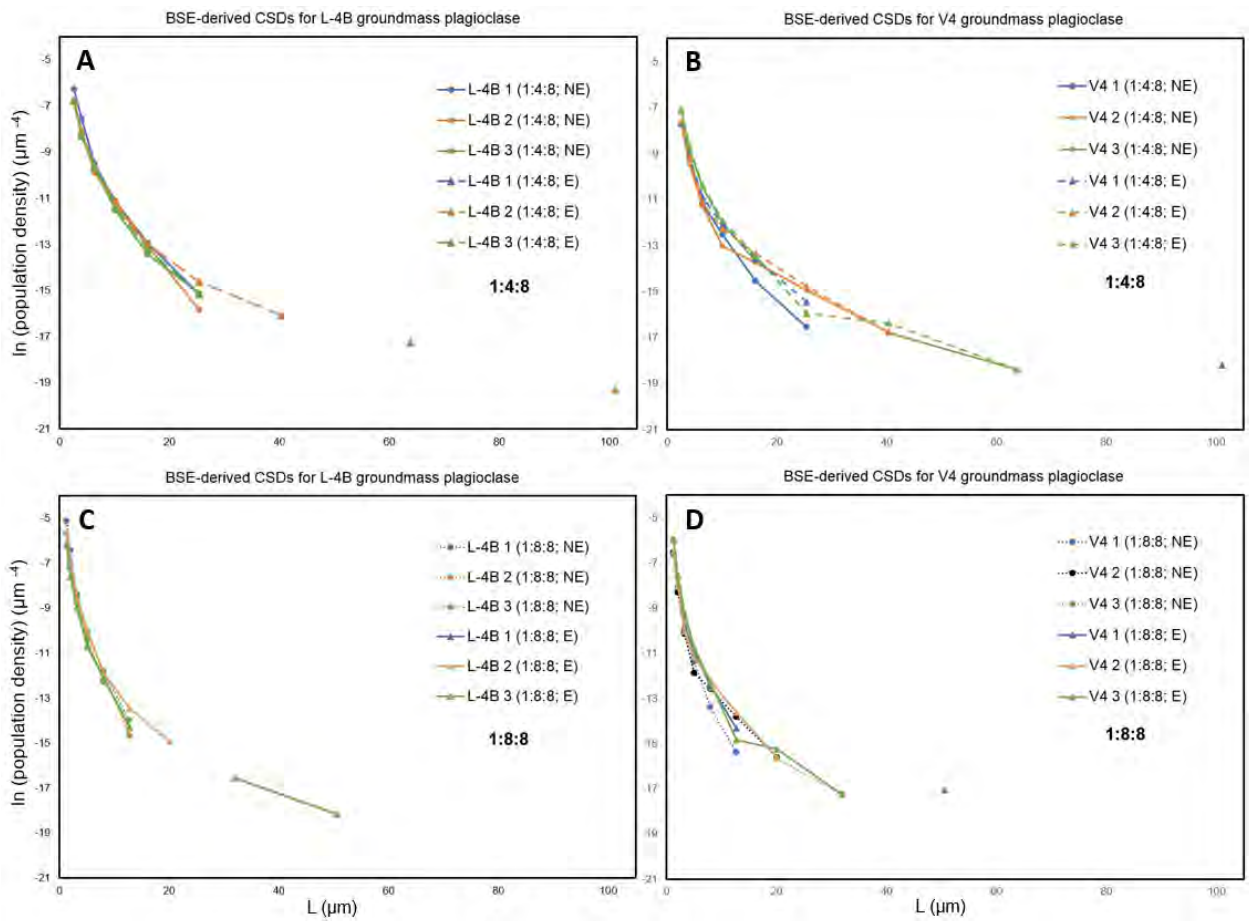

DOI: https://doi.org/10.2138/am-2020-7007

Figure 5

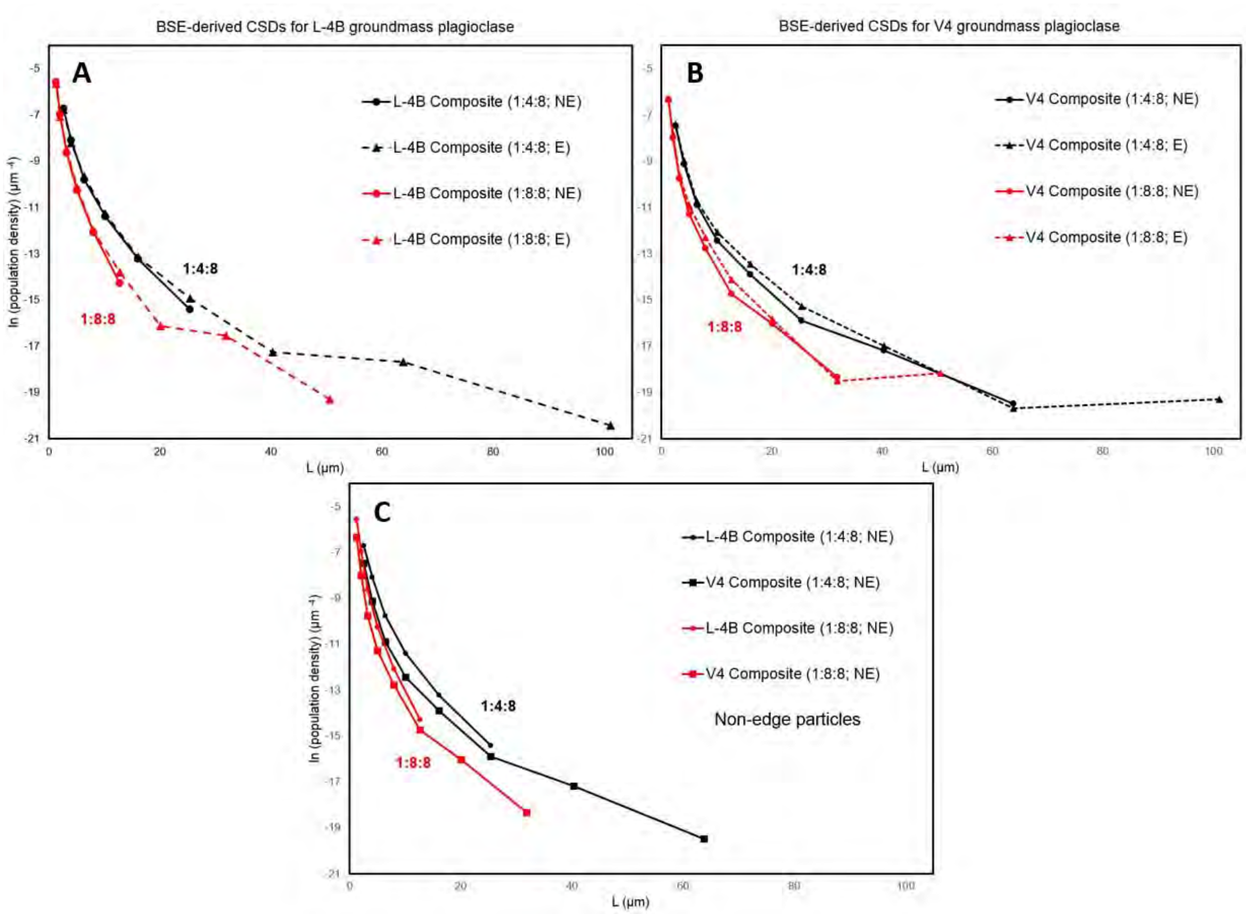

Figure 6

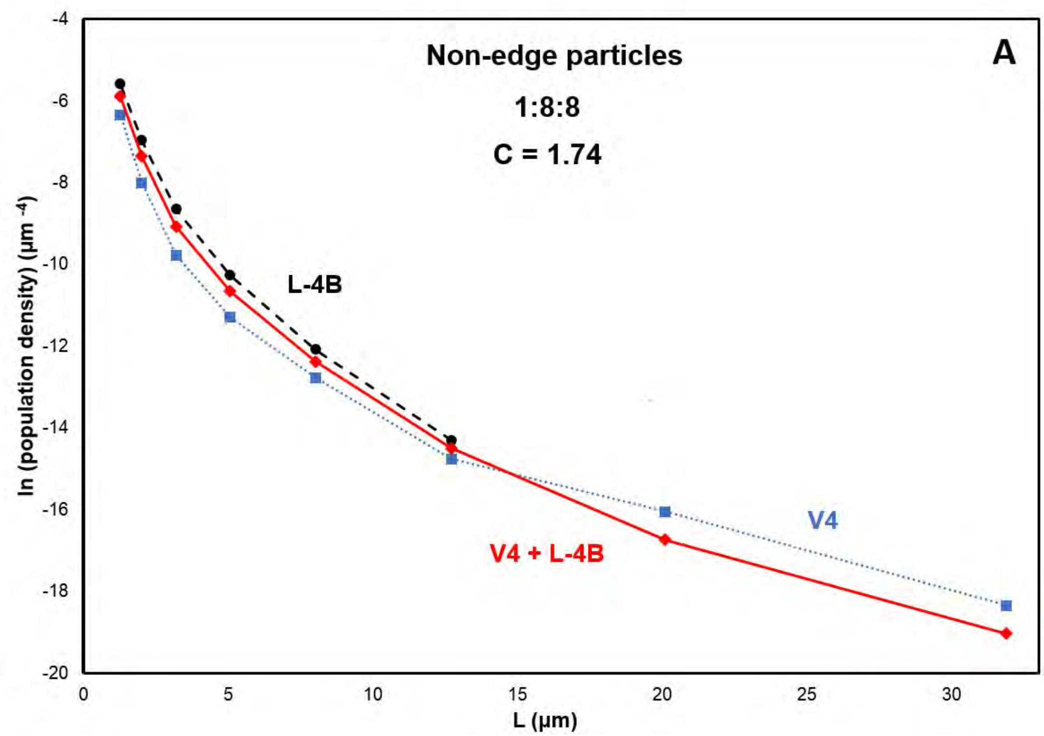
Non-edge particles
1:8:8
C = 1.74
A
L-4B
V4
V4 + L-4B
ln (population density) (μm -4)
L (μm)
-4
-6
-8
-10
-12
-14
-16
-18
-20
0
5
10
15
20
25
30

1205 Figure 7

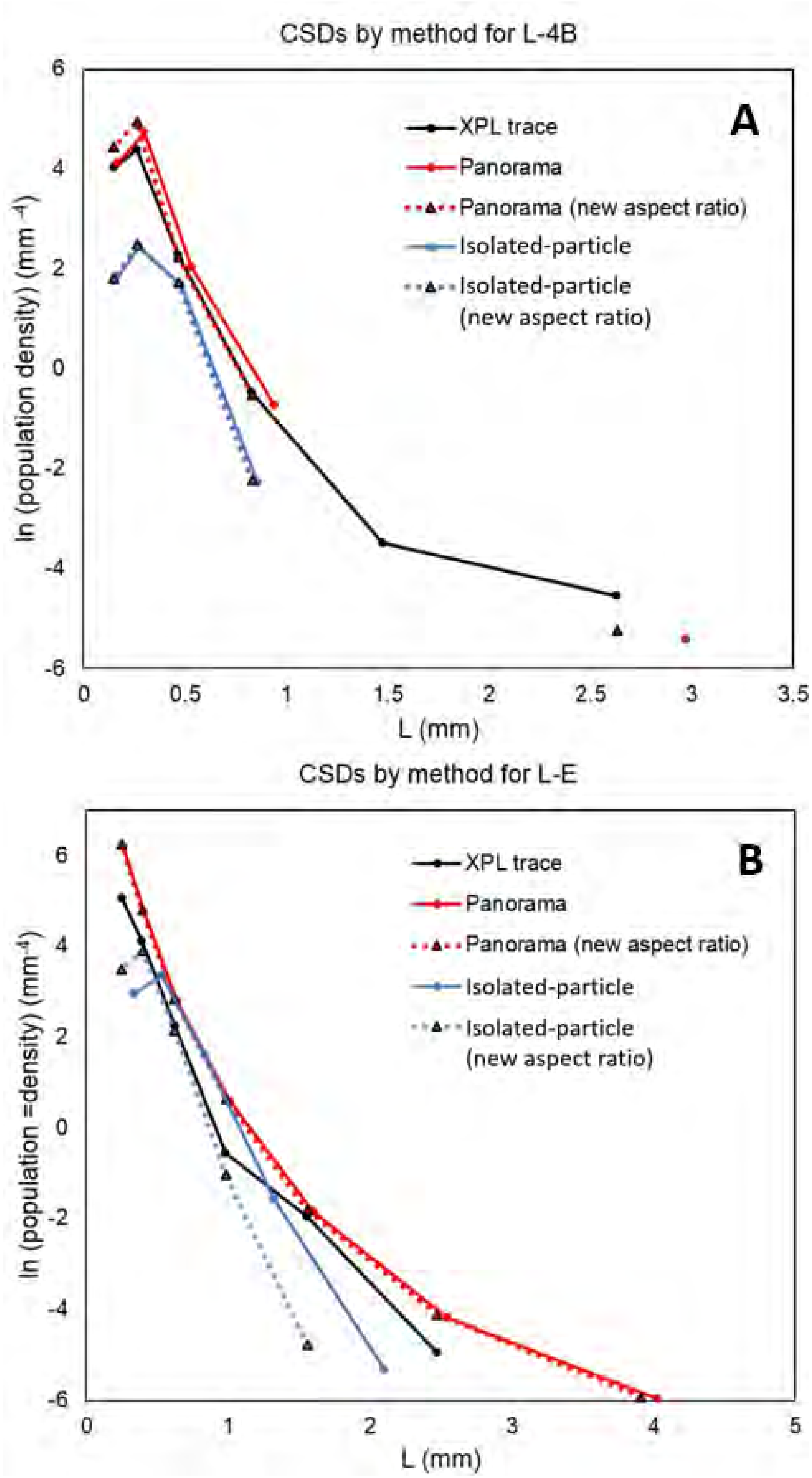

1206

Figure 8

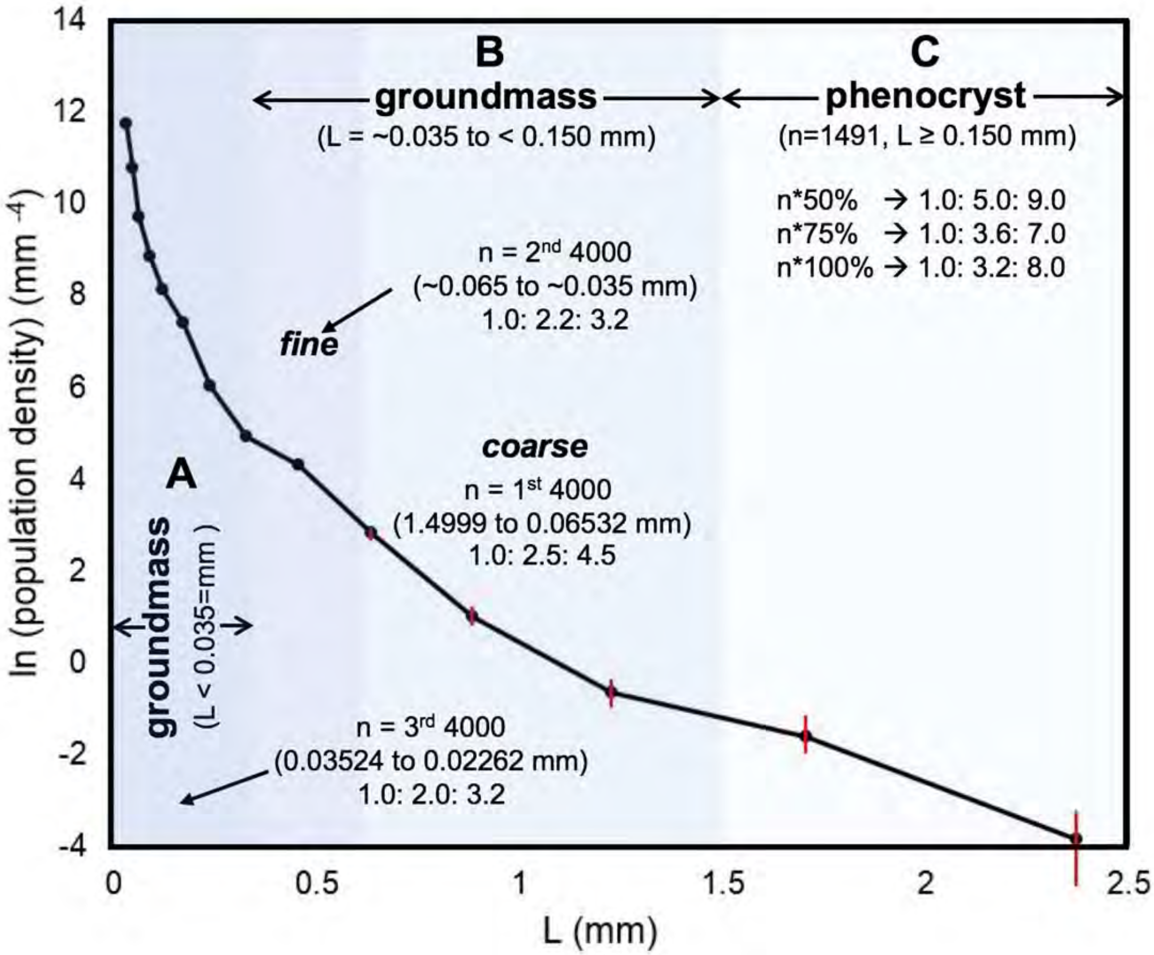
B
groundmass
(L = ~0.035 to < 0.150 mm)
C
phenocryst
(n=1491, L ≥ 0.150 mm)
n*50% → 1.0: 5.0: 9.0
n*75% → 1.0: 3.6: 7.0
n*100% → 1.0: 3.2: 8.0
n = 2nd 4000
(~0.065 to ~0.035 mm)
1.0: 2.2: 3.2
fine
coarse
n = 1st 4000
(1.4999 to 0.06532 mm)
1.0: 2.5: 4.5
A
groundmass
(L < 0.035=mm)
n = 3rd 4000
(0.03524 to 0.02262 mm)
1.0: 2.0: 3.2
ln (population density) (mm -4)
L (mm)

Figure 9